Master's thesis

NTNU
Norwegian University of Science and Technology
Faculty of Natural Sciences
Department of Physics

Elise Wright Knutsen

Dynamical-Chemical Coupling in the Polar Middle Atmosphere

Effects of Energetic Particle Precipitation on the Middle Mesospheric Maximum

Master's thesis in Physics
Supervisor: Patrick J. Espy
May 2019

Marie Henriksen

NTNU
Norwegian University of
Science and Technology

Elise Wright Knutsen

Dynamical-Chemical Coupling in the Polar Middle Atmosphere

Effects of Energetic Particle Precipitation on the Middle Mesospheric Maximum

Master's thesis in Physics
Supervisor: Patrick J. Espy
May 2019

Norwegian University of Science and Technology
Faculty of Natural Sciences
Department of Physics

NTNU
Kunnskap for en bedre verden

Acknowledgements

Many thanks to my supervisor Prof. Patrick Espy, for all his insights and advice, enthusiasm and encouragements. My passion for planetary science was born out of his excellent classes, and his sense of humor and endless digressions made the last year at NTNU the best of them all.
I also want to thank Dr. Stefan Bender for helpful input, advice and feedback, and for lending a hand in unfamiliar data territory.
Thanks to Marie Henriksen, for all the fun times, and for providing the fantastic photo on the cover of this thesis.
Lastly I thank you Astri, roommate for six years and best friend, for the infinite amount of high-fives.

Abstract

The middle mesospheric ozone maximum is a recently discovered feature in the winter polar atmosphere. Geomagnetic activity is thought to play a role in the middle atmospheric ozone budget, and possibly affect weather and climate via energetic particle precipitation. The objective of this thesis is to quantify the extent to which particle precipitation changes ozone concentrations between $50-75$ km, with focus on the middle mesospheric maximum. The ground-based radiometer of the British Antarctic Survey at Troll station in Antarctica and NASAs EOS Aura satellite provide ozone profiles for three consecutive Antarctic winters. Geomagnetic indices AE and Dst are used to identify times of enhanced geomagnetic activity and act as proxies for particle precipitation. Time series of ozone and geomagnetic indices are gathered in a super posed epoch analysis, and cross-correlation analysis is performed on these epochs. Results show a relative decline in ozone of 2-3 times compared to normalized background levels following moderate to strong geomagnetic storms. The correlation coefficient between O_3 and Dst and O_3 and AE for the same storm level was found to be 0.6 and -0.45 respectively, indicating that AE (computed solely from northern hemisphere measurements) is not optimal for identification of precipitation events in the southern hemisphere. The equatorial ring current seems to precipitate symmetrically with respect to the hemispheres, making it a good proxy for particle precipitation over both poles. The ozone depletion is seen to reach altitudes down to 55 km almost immediately after storm peak, and recovers on the time scale of 2-4 days. The lack of temporal diffusion of the ozone depression indicates catalytic ozone destruction primarily by odd-hydrogen species, created by energetic radiation belt particles. The absence of a more time delayed depletion suggests downward transport of odd-nitrogen from the thermosphere or upper mesosphere happens rarely.

Sammendrag

Det midtre mesosfæriske ozonmaksimum er et nylig oppdaget fenomen, som finner sted i atmosfæren over polområdene vinterstid. Geomagnetisk aktivitet er kjent for å spille en viktig rolle i den midtre atmosfærens ozonbudsjett, og kan påvirke både vær og klima gjennom energisk partikkelutfelling. Målet med denne oppgaven er å kvantisere i hvilken grad partikkelutfelling endrer ozonkonsentrasjonen mellom 50 km-75 km, da med spesielt fokus på det midtre mesosfæriske ozonmaksimum. *British Antarchtic Survey* sitt bakkebaserte radiometer, som er stasjonert ved den norske stasjonel Troll, og NASA sin satelitt *EOS Aura*, har begge gitt kontinuerlige ozonprofiler gjennom tre påfølgende vintre. De geomagnetiske indeksene AE og Dst har blitt brukt til å identifisere tidspunkt med forhøyet geomagnetisk aktivitet. Indeksene ble på denne måten brukt som indikator for energisk partikkelutfelling. Tidsserier av ozon og de geomagnetiske indeksene ble samlet i en *superposed epoch*-analyse, og kryss-korrelasjon-analyse ble gjennomført på disse epokene. Resultatene viser en relativ reduksjon i ozon på 2-3 ganger, kort tid etter en moderat til sterk geomagnetisk storm, sammenlignet med det normaliserte bakgrunnsnivået av mesosfærisk ozon. Korrelasjonskoeffisienten mellom ozon og Dst, og ozon og AE, for samme stormstyrke ble kalkulert til henholdsvis 0.6 og -0.45. Dette indikerer at AE, som er basert på målinger utelukkende fra den nordlige halvkule, ikke er en optimal indikator av partikkelutfelling over den sørlige halvkule. Den ekvatoriale ringstrømmen ser ut til å utfelle partikler tilnærmet symmetrisk over begge halvkuler, noe som gjør Dst-indeksen til en bedre indikator for partikkelutfelling over begge polene. Resultatene viser at ozonreduskjonen når helt ned til 55 km omtrent umiddelbart etter stormmaksimum og at ozonnivået for det meste er gjenopprettet innen 2-4 dager. Mangelen på utstrekning av ozonreduksjonen i tid indikerer katalytisk ozonødeleggelse, hovedsakelig som følge av odd-hydrogenmolekyler, produsert av energisk strålingsbeltepartikler. Fraværet av en tidsforsinket eller tidsutstrukket ozonredusksjon tyder på at nedadgående transport av odd-nitrogen fra termosfæren eller øvre mesosfære sjeldent skjer.

Contents

List of acronyms

AE	Auroral electrojet index
AL	Auroral electrojet lower
AO	Auroral electrojet equivalent zonal current
AP	Auroral particles
AU	Auroral electrojet upper
BAS-MRT	British Antarctic Survey Microwave Radiometer at Troll
Dst	Disturbance storm time index
EPP	Energetic particle precipitation
EPP-DE	Energetic particle precipitation direct effect
EPP-IE	Energetic particle precipitation indirect effect
FAI	The Fédération Aéronautique Internationale
FUV	Far-ultraviolet
HSS	High speed streams
IMF	Interplanetary magnetic field
MLS	Microwave Limb Sounder (on EOS Aura satellite)
MMM	Middle mesospheric maximum
NH	Northern hemisphere
NH-AE	Northern hemisphere auroral electrojet index
NOAA	National Oceanic and Atmospheric Administration
RBP	Radiation belt
SEP	Solar energetic particles
SEA	Superposed epoch analysis
SH	Southern hemisphere
SH-AE	Southern hemisphere auroral electrojet index
SZA	Solar zenith angle

1 Introduction

The tertiary ozone maximum was first described in 2001 by Marsh et al. (2001). Since then several papers (Hartogh et al. (2004), Sofieva et al. (2009), Daae et al. (2013), Smith et al. (2018)) have discussed its magnitude and spatial and temporal properties. The middle mesospheric maximum (MMM) exists between $60-75\,\mathrm{km}$ at high latitudes as a result of a temporary change in ozone sinks relative to ozone production. In polar regions during summer months, there is a deep ozone minimum between the stratospheric primary ozone layer and the upper mesospheric secondary layer. As winter approaches, the upper atmosphere is no longer continuously illuminated by the entire UV spectrum. UV radiation of shorter wavelengths are attenuated more than the longer far-UV (FUV) photons which leads to a reduction in the photolysis of water vapour, resulting in less production of odd-hydrogen species known as HO_x. HO_x gases, along with NO_x, are known to catalytically destroy ozone. The wavelengths needed to produce ozone are longer and are still able to penetrate the optically thick atmosphere even during winter. And so for a limited time, more ozone is created than is destroyed and the middle mesospheric maximum emerges.

Energetic particle precipitation (EPP) may occur at times of enhanced geomagnetic activity. The Disturbance storm time (Dst) and Auroral Electrojet (AE) indices are widely used to indicate the level of geomagnetic activity, providing a scale to geomagnetic storms. EPP produce HO_x and NO_x through ionization processes, and studies looking at the ozone response of the MMM after a single occurrence of increased EPP, report an increase in local HO_x and/or NO_x accompanied by a decrease in O_3 (e.g. Daae et al. (2012), Verronen et al. (2006)). Changes in the atmospheric ozone content could alter temperatures and zonal winds, as reported by Jackman et al. (2007). It is therefore imperative that the coupling of space weather and the atmosphere is included in climate models.

Evidence suggests that solar variability and climate are interconnected. Still, the scientific understanding of atmospheric processes related to solar forcing remains very low, according to the Intergovernmental Panel on Climate Change. The middle atmosphere is a complex system however, and changes in temperature, humidity, chemistry, dynamics as well as solar forcing could alter the ozone content. As the lifetime of mesospheric ozone is short, daily observations of ozone over long time periods are required to determine the effect of energetic particle precipitation on mesospheric ozone.

This study aims to quantify the extent to which EPP changes ozone concentration in the middle mesosphere. Geomagnetic indices AE and Dst are used as proxies for particle precipitation to identify storms during a three year time period where the level of geomagnetic activity required to observe an effect on O_3 is determined. At last the suitability of the indices for this type of study is evaluated.

This thesis examines the middle mesosphere in specific, but the atmosphere in general is also discussed. Atmospheric composition, structure and dynamics is presented before the tertiary maximum is described in detail. Background theory on the solar wind and its interactions with the terrestrial magnetosphere is also presented. The results from the superposed-epoch and correlation analysis is described, followed by a discussion and finally a summary with concluding remarks.

2 Theory

2.1 The atmosphere

The terrestrial atmosphere is the layer of gas surrounding our planet. It constitutes less than one millionth of the mass of the Earth, while also being essential for all life. The atmospheric layers provide pressure for water to remain liquid at the surface, absorb hazardous UV radiation and provide a tepid climate via greenhouse gases. Without it, life as we know it would not be feasible.

The middle atmosphere, and the mesosphere in particular, is very interesting due to its position between two completely differently behaving regions. Below the mesosphere the atmosphere is dynamical and well mixed, and above it is ionized and molecular diffusion dominates. The mesosphere is affected by both regions, and constantly slides from one regime to another, which leads to complex interactions between heating, photochemical reactions and dynamical phenomena. Understanding the nature of the middle atmosphere can improve on climate models, since the role solar particles play in climate forcing is still not completely understood. This chapter is mostly based on Andrews (2010) and will provide a brief overview of the characteristics of the atmosphere in general, and the mesosphere in specific.

2.1.1 Composition

The atmosphere contains several different gases and aerosol particles. The gases are defined by their abundance and lifetime in a system. The amount of a gas in a system can be expressed in several ways, the most commonly used is concentration (kgm^{-3}), and volume mixing ratios (m^3 gas per m^3 air). Minor constituents, or trace gases, are more often given in units of parts per million (or billion, trillion aso.) volume, or ppmv (or simply ppm). Even though trace gases amount to an almost insignificant number in total atmospheric volume, they play a crucial role in heat transfer processes in the atmosphere. An overview of the constituents of the Earth's atmosphere is given in table 1.

Name (formula)	Concentration	Lifetime
Nitrogen (N_2)	78.08%	1.6×10^7 years
Oxygen (O_2)	20.95%	3×10^3-10^4 years
Argon (Ar)	0.934%	constant
Water vapour* (H_2O)	0-4%	10 days
Carbon dioxide (CO_2)	430 ppmv	20-150 days
Neon (Ne)	18.18 ppmv	constant
Helium (He)	5.24 ppmv	10^7 years
Methane (CH_4)	1.79 ppmv	10 years
Krypton (Kr)	1.14 ppmv	constant
Hydrogen (H_2)	0.53 ppmv	2 years
Nitrous oxide (N_2O)	0.325 ppmv	150 years
Carbon-monoxide (CO)	$\sim$ 0.2 ppmv	0.2-0.5 years
Xenon (Xe)	0.087 ppmv	constant
Ozone (O_3)	$\sim$ 0.6 ppmv	weeks-months
Nitrogen-dioxide (NO_2)	$\sim$ 0.25 ppmv	8-10 days

Table 1: Main constituents of the dry atmosphere. *Concentration of water vapour is not included in dry atmosphere. Percent by volume.

The amounts of these gases vary with altitude, due to seasonal effects, time of day, human emissions, volcanic eruptions and other sudden events. 90% of all water vapour is contained to the lower 5 km of the atmosphere, and the majority of the ozone is located at about 30 km. The vertical composition of gases is well mixed up to about 80 km, where the turbopause is located. The region below the turbopause is called the homosphere. Here, there is no significant change in composition. Above the turbopause is the heterosphere, where gases are separated by their molecular mass, and above 100 km the gases are mostly ionized.

2.1.2 Vertical structure

There is no clear boundary separating the atmosphere and outer space. The Fédération Aéronautique Internationale (FAI), an international organization founded in 1905 and has 104 active and associate member countries, maintains records and definitions regarding spaceflight and aeronautics. FAI defines the limit between atmosphere and space at the Kármán line (100 km). At this altitude, a vehicle would have to travel faster than the orbital velocity to create enough aerodynamic lift to sustain itself. At this altitude, the atmospheric pressure has dropped to less than 0.001 mbar.

The atmosphere is divided into five main regions where each region is distinguished from its neighbours by the vertical temperature profile. The exact lower and upper limits of all these layers vary with season as well as latitude. Figure 1 shows an overview of the location of the four lower layers and their general temperature trends.

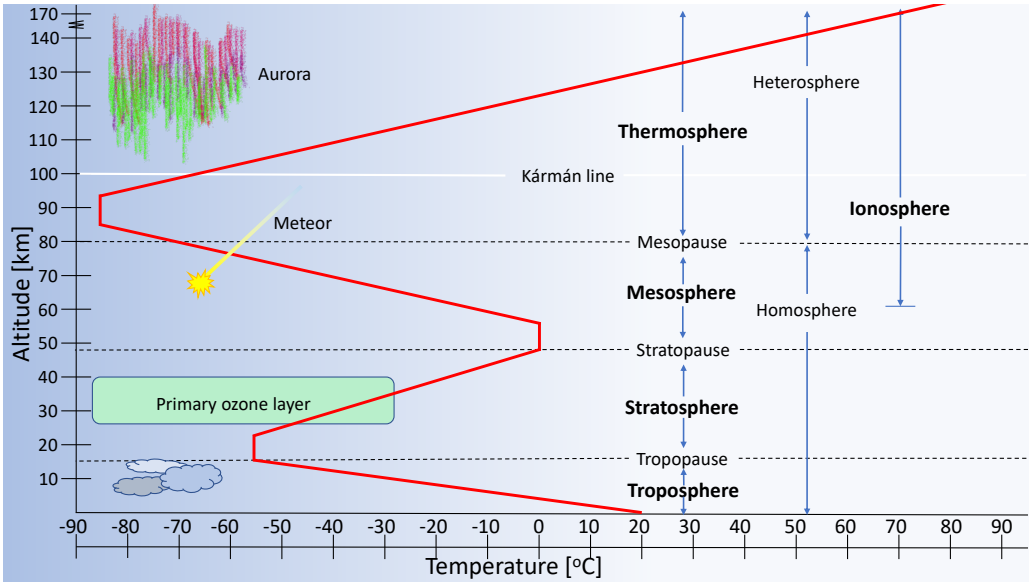

Figure 1: Vertical structure of the atmosphere at equator, including all layers and boundary regions with temperature profile shown in thick red line.

Density and air pressure generally decrease with height, but temperature can remain constant and even increase in certain regions. The pattern remains constant however, and is therefore used as a metric to distinguish the layers. Every layer is separated from the next by a change of sign of the temperature gradient.

The bottom layer is called the troposphere, it is dominated by heating from the ground, which results in the temperature drop as a function of height. The troposphere reaches up to about 15 km (higher in the tropics and lower in the polar regions), it contains close to 75% of the total atmospheric mass, as well as the most common atmospheric phenomena, such as clouds. It ends in the tropopause, where the increase in photolysis of ozone produces the next layer, the stratosphere, have a positive temperature gradient. This ozone forms the stratospheric ozone layer, which was partially depleted during the last half of the 20th century due to human emissions of CFCs. This ozone layer protects all life on Earth by absorbing UV radiation, preventing DNA damage.

The stratosphere is followed by the stratopause where again the temperature gradient changes. Next follows the mesosphere where the temperature decreases with altitude. Noctilucent clouds, cloud-like structures made of ice particles that form on tiny dust particles, possibly originating from micrometeors, are found in the mesosphere. The upper part of the mesosphere is part of the ionospheric D-layer, and is partly ionized during the day. When the Sun dips below the horizon and the source of ionization disappears, the ions and their free electrons recombine to form neutral molecules. This region is hard to study; jets and balloons don't go high enough, and satellites and space shuttles orbit too high.

The mesopause is the coldest region of the Earth's atmosphere due to radiative cooling by CO_2, reaching temperatures below $-143\,°C$. The summer mesospheric pole is especially interesting as it is much colder than the winter mesosphere. The cold conditions at the summer pole are maintained by a constant upwelling of air which is part of a global circulation system comprised of upwelling at the summer pole, horizontal motion from summer to winter pole, followed by a downwelling at the winter pole (see figure 2), more

on this in section 2.1.3.

The stratosphere, mesosphere and lower part of the thermosphere is considered the middle atmosphere, spanning from $\sim$ 15 km to 100 km. Below the mesopause, all atmospheric constituents are well-mixed, and are therefore part of the homosphere (see figure 1). The thermosphere is considered part of Earth's atmosphere, but air density here is extremely low, and most of the thermosphere is above the Kármán line which is why the middle and upper thermosphere in some cases is also considered outer space. The gases in the thermosphere are not well-mixed, and sort themselves into layers according to their molecular mass. High energy UV radiation from the Sun ionize the gases, increasing the temperature as with altitude.

The thermosphere often overlaps with the remaining ionosphere, namely the E and F-regions. The F-region can be found anywhere between $150-800$ km depending on solar forcing. The ionosphere generally extends higher than the thermosphere, reaching altitudes of around 1000 km, while the thermosphere is often said to end at $\sim$500 km.

Beyond the thermosphere is the uppermost layer of the atmosphere; the exosphere. This region gradually fades into the vacuum of space. The molecules here are bound to Earth by gravity, but the density is far too low for the molecules to behave as a gas. In principle the upper boundary of the exosphere is where solar radiation pressure takes over from gravity as the dominating force acting on atomic hydrogen. This occurs close to the orbit of the Moon on the Sun facing side $\sim$400 000 km. On the night side, recent research has found that the exosphere extends as far back as 640 000 km (Baliukin et al., 2019).

2.1.3 Dynamics

To maintain a constant temperature, the Earth has to radiate away and absorb equal amounts of energy. The difference in absorption of solar radiation in the tropics and at the poles due to geometrical factors, is the main cause of the large-scale pole-equator circulations observed in the atmosphere.

Due to the rotation of the Earth, the composition of the atmosphere as well as topological features, the general circulation does not follow a direct poleward flow but instead circulates in a complicated set of patterns. At lower altitudes, these patterns form what is called cells.

There are three large cells encircling the planet in each hemisphere; the Hadley cell near the equator, the Ferrel cell at mid-latitudes and the Polar cell. The purpose of these three cells is to redistribute heat which is unevenly impacting on the Earth. Both the Hadley and the Polar cell are direct consequences of the surface temperature of the planet, while the Ferrel cell exists as a result of its two neighbours. The Ferrel cell is weaker than the other two, as it has neither a strong source nor sink of heat.

The Polar cell is a fairly simple system; driven by convection it moves hot air from the equatorial regions towards the poles where heat radiates into space. The Polar cell radiates away more heat than it receives, acting as a heat sink. Hadley cell behaves oppositely, as it receives more heat than it radiates away and acts as a heat source.

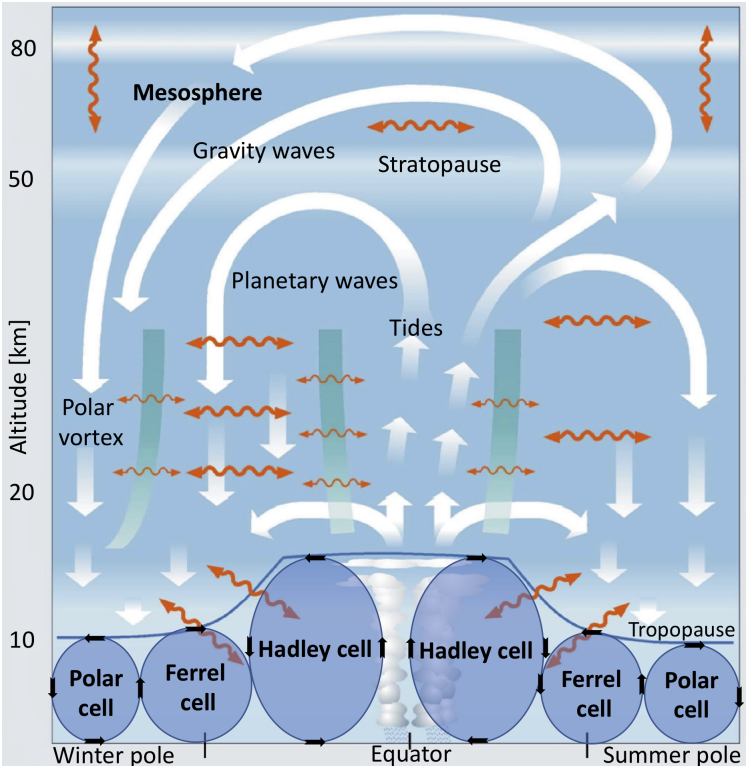

Figure 2: Atmospheric circulation, showing Hadley, Ferrel and Polar cells in both hemispheres, and the overarching Brewer-Dobson circulation as thick white arrows. Orange arrows indicate heat transfer. Figure adapted from Bönisch et al. (2011).

The Brewer-Dobson circulation is found at higher altitudes, but it still interacts with the three cells below, depicted in figure 2. Dobson et al. (1929) postulates a slow wind current in the stratosphere, redistributing warm tropical air into the winter hemisphere. The Brewer-Dobson circulation is driven by planetary waves breaking in the winter stratosphere, causing the air to cool and sink. This air needs to be replaced by air from the tropics. In summary a meridional circulation is formed, with air rising in the tropics and sinking in the winter polar region.

Large air masses of low pressure and temperature rotates counter-clockwise around the winter pole at stratospheric altitudes. These jets create the polar vortices, driven by the extreme temperature differences between the winter pole and equator. The strong jets filter out westward waves in the summer and eastward waves in the winter. To conserve energy, gravity waves that make it through this filtering grow in amplitude as they propagate upwards into less dense atmosphere. At mesospheric altitudes they eventually break, deposit their momentum and affect global circulation. Due to this filtering, the asymmetric spectrum of waves in the mesosphere force the polar vortex to reverse direction in the mesosphere (Smith et al., 2011). Downward transport of trace species like NO_x from the thermosphere through the mesopause and into the mesosphere is therefore uncertain. The polar vortices break up when spring comes to the winter pole.

2.2 Middle mesospheric ozone

Ozone is an unstable triatomic form of oxygen, created naturally by photodissociation of O_2. Its distribution varies with altitude, time and location due to dynamical and chemical processes. Ozone is distributed within three distinct ozone maximums, the exception being ozone below 10 km originating from human emissions. The largest, and by far the most well-known, ozone maximum is the stratospheric ozone layer, containing approximately 90% of all atmospheric ozone. This layer is also called the primary ozone layer, and during Antarctic winters it peaks at values of ∼6 ppmv. Near the mesopause at ∼90 km the secondary layer is located, with a slightly lower density of ∼4.5 ppmv. The much smaller tertiary ozone maximum, henceforth denoted the middle mesospheric maximum (MMM), is a highly localized phenomenon. It only exists in polar regions around the day-night terminator during winter months, reaching densities of 2-3 ppmv.

The first measurements of the middle mesospheric maximum were carried out by Froidevaux et al. (1996), using the MLS instrument (Microwave Limb Sounder) on the UARS (Upper Atmosphere Research Satellite) in 1992, and was described by Marsh et al. (2001). Figure 3 shows ozone profiles for different latitudes, clearly confirming the existence of a tertiary maximum between 60 −70 km at higher latitudes.

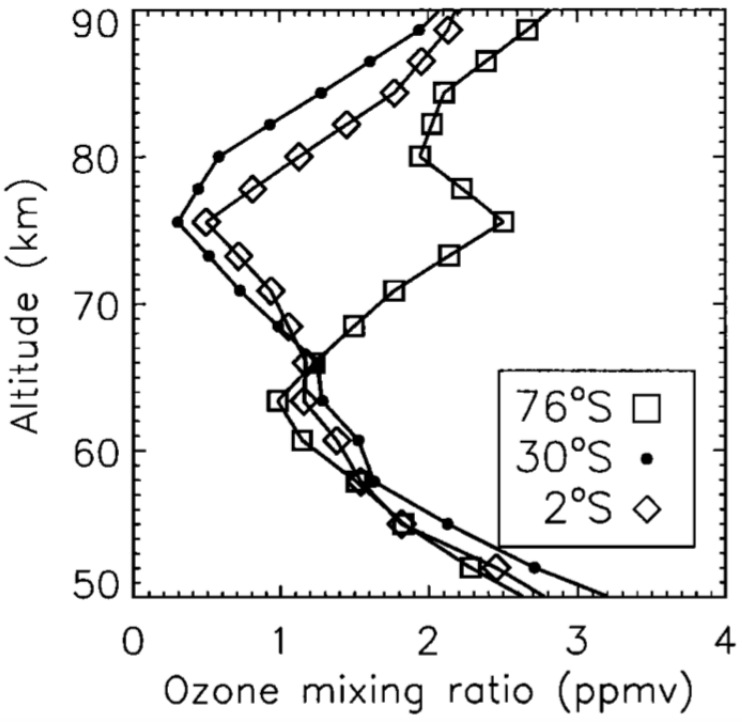

Figure 3: Mean ozone profiles from MLS on board the *Upper Atmosphere Research Satellite* for different latitudes. Profiles taken during nighttime between August 16th and 21st, 1992. From Marsh et al. (2001).

Atmospheric ozone is measured in situ with air samples by balloon, and by remote sensing techniques from ground-based instruments, with low- and high-altitude aircraft as well as by satellite. One can observe ozone either by its absorption of UV, infrared or visible light, or by its emission of microwave or infrared radiation. Emission instruments

have the advantage of providing measurements at night and during polar winters (BAS, 2018).

2.2.1 Ozone chemistry

Sidney Chapman was the first to correctly explain the ozone cycle in the middle atmosphere (now known as the Chapman cycle), postulating that atmospheric ozone is created when solar UV radiation dissociates an oxygen molecule to produce two oxygen atoms. Next, each atom combines with an oxygen molecule to produce an ozone molecule, see equations 2.1 and 2.2.

$$O_2 + h\nu_s \rightarrow 2O \tag{2.1}$$

$$O + O_2 + M \rightarrow O_3 + M \tag{2.2}$$

In the above equation, M is an inert third body stabilizing the reaction. ν_s represents wavelengths in the Herzberg continuum ($185-242\,\text{nm}$) and the Schuman-Runge system ($170-200\,\text{nm}$). These reactions occur continuously whenever solar UV radiation is present. As a result, the greatest ozone production occurs in the tropical stratosphere (Andrews, 2010).

The production is balanced by the destruction of ozone by combination with atomic oxygen as in equation 2.3, or photolysis in equation 2.4.

$$O_3 + O + M \rightarrow 2O_2 + M \tag{2.3}$$

$$O_3 + h\nu_l \rightarrow O_2 + O \tag{2.4}$$

In order to photodissociate ozone, wavelengths $\lambda_l > 1140\,\text{nm}$ are required. As a result, the MMM is largely diurnal in nature. Ozone is continuously formed at night by the recombination of atomic oxygen created during the day, and is turned back into molecular oxygen when illuminated.

What Chapman did not correctly predict is the total distribution of ozone in the atmosphere, as he did not take into account the transport of odd-oxygen, or the catalytic destruction of ozone in equation 2.3. These catalytic cycles are important features in the ozone budget, and are mainly caused by odd-hydrogen (HO_x), odd-nitrogen (NO_x), Chlorine (Cl) and Bromine (Br). HO_x and NO_x are groups of species; $HO_x = H + OH + HO_2$ and $NO_x = N + NO + NO_2$. All of them occur naturally in the atmosphere to some extent, but 30% of all bromine and 80% of chlorine comes from human emissions.

An example of a catalytic cycle, where X is the catalytic species, is as follows:

$$X + O_3 \rightarrow XO + O_2 \tag{2.5}$$

$$XO + O \rightarrow X + O_2 \tag{2.6}$$

The net effect being a reduction in ozone and atomic oxygen, and no change in the catalytic species.

In the lower/middle mesosphere, the catalytic species HO_x is mainly created by photolysis of water vapour (equation 2.7).

$$H_2O + h\nu \rightarrow H + OH, \tag{2.7}$$

The wavelengths required to photodissociate water vapour are in the Schuman-Runge and Lyman-α bands. The dissociation is dominated by Schuman-Runge below 70 km, and by Lyman-α above 70 km (Minschwaner et al., 2011).

Odd-oxygen ($O_x = O + O_3$) is needed to produce ozone, as seen in equation 2.2, so an increase in HO_x is dampening the overall ozone production. An important reaction leading to O_x loss is a hydroxyl cycle described by (Marsh et al., 2001):

$$O + OH \rightarrow O_2 + H \tag{2.8}$$

$$O_2 + H + M \rightarrow HO_2 + M \tag{2.9}$$

$$HO_2 + O \rightarrow O_2 + OH \tag{2.10}$$

The net result becomes an increase of molecular oxygen and a decrease of atomic oxygen, leading to a decrease in ozone production.

HO_x and NO_x do appear naturally in the mesosphere, but during times of enhanced geomagnetic activity the levels of these catalytic molecules can see a drastic increase, altering the atmospheric chemistry (Sinnhuber et al., 2012). More details about the effects of EPP can be found in section 2.4.1.

2.2.2 Ozone and solar zenith angle

The moving line separating the illuminated side of the planet from the dark side is called the terminator. An observer standing on this line would experience twilight due to the scattering of incoming light on the atmosphere above. Seen as a whole the terminator is a circle with a diameter approximately equal to the Earth's. The circle passes through every point on the Earth twice per day, except the polar regions when they experience polar night or midnight sun.

The solar zenith angle (SZA) is defined as the angle between vertical and the Sun's position. It is at a minimum at noon and at slightly more than 90° at sunrise and sunset due to atmospheric refraction. It also depends on latitude and day of year. During polar winters the Sun is below the horizon continuously, and the zenith angle is greater than 90° for many weeks. In this thesis, night will be defined as SZA $>=$ 100° (or solar elevation angle $< -10°$).

Figure 4 shows how ozone averaged over days 18-23 for each month behaves as a function of solar elevation angle.

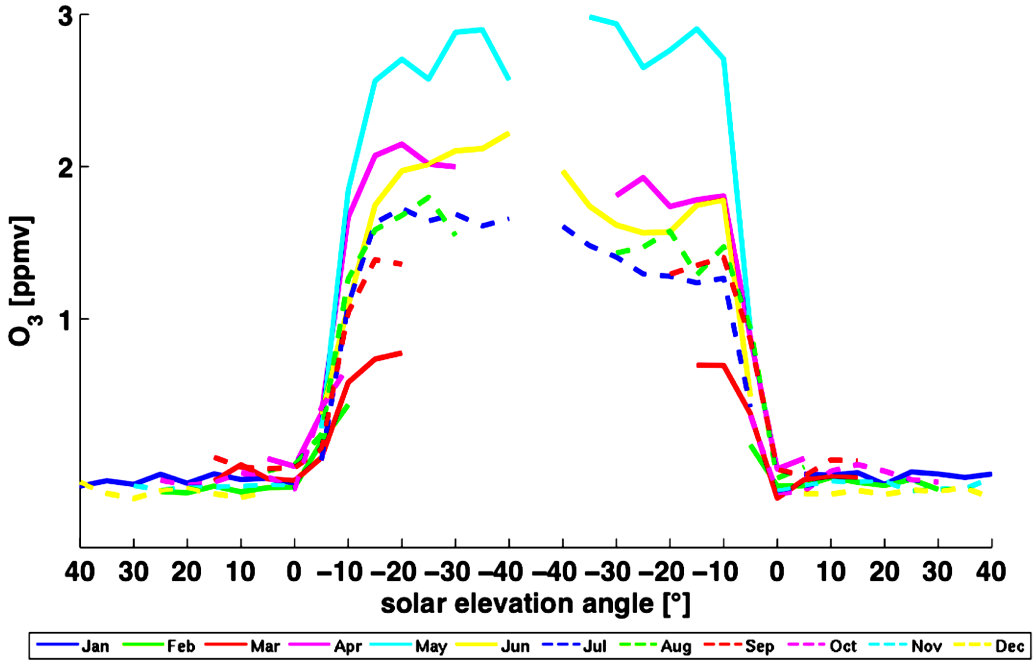

Figure 4: Ozone on days 18-23 of each month averaged over solar elevation angle. Figure from Kleinknecht (2015).

The MMM behaves in this way due to the absorption and scattering of incoming solar rays in the FUV, a consequence of large zenith angles. When the solar zenith angle is large, a stronger decline of the dissociation rate of water vapor is observed compared to that of molecular oxygen, as shown in figure 5. The increased rates of dissociation of O_2 leads to higher ozone production as the SZA increases.

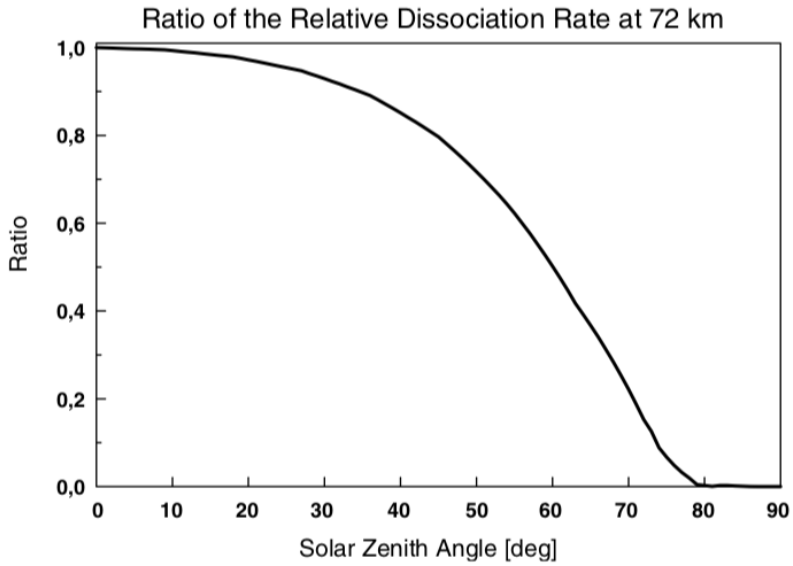

Figure 5: Ratio of the relative dissociation rates of water vapor to molecular oxygen. Figure from Sonnemann et al. (2006).

The Lyman-α radiation determines the photolysis rate of water vapour at higher altitudes (above 70 km), while the Schuman-Runge bands are responsible for a small production of ozone close to the polar night terminator, which results in an ozone accumulation large enough to feed the MMM through the polar night (Sonnemann et al., 2006).

The MMM is observable at night from mid March until mid October in the southern hemisphere, and from October to April in the northern hemisphere as depicted in figure 6.

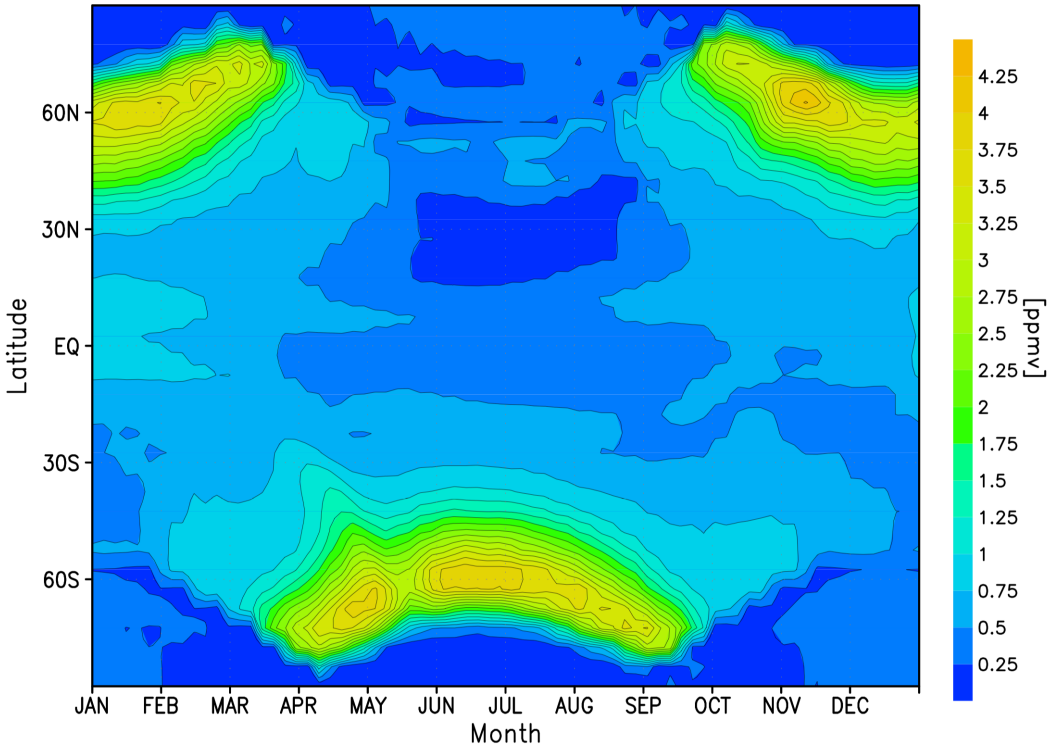

Figure 6: Modelled contour plot of ozone volume mixing ratio at 72 km as a function of latitude and time of year. Figure from Hartogh et al. (2004).

Geographically the MMM can be observed in a 15° latitude band around the terminator, reaching into the mid-latitudes at night, (Hartogh et al., 2004). The MMM does not reach further poleward of the terminator due to the very large SZA in this region. O_3 losses are suppressed as no ultraviolet radiation is no longer present but so are the sources, as FUV is needed to dissociate O_2 to create atomic oxygen.

The maximum does not extend into the mesopause or connect to the secondary ozone layer because the low air density results in almost no conversion of H into H_2O. This leads to a a substantial increase in H, and the destruction of ozone through the reaction shown in equation 2.11.

$$H + O_3 \rightarrow OH + O_2 \tag{2.11}$$

Increased levels of atomic hydrogen inhibits an accumulation of ozone around 80 km (Hartogh et al., 2004). Neither is the MMM seen closer to the stratopause where the main source of odd-hydrogen is the reaction between excited atomic oxygen and water vapour. To reach the stratosphere for large SZA, photons travel through the troposphere which is optically thin for the wavelengths required to create the excited oxygen ($\lambda < 310$ nm).

In this way, OH is still produced near the polar night terminator, preventing the middle mesospheric maximum from extending downward.

2.2.3 Ozone transport

Most of the total ozone content in the atmosphere is created near the equator where the solar flux is strongest. Stratospheric wind patterns move air to higher latitudes, transporting ozone towards the poles. The Antarctic mesosphere is dominated by planetary waves, gravity waves and tides (see figure 2). These waves originate from lower regions in both altitude and latitude, coupling the mesosphere to the rest of the atmosphere. The mesosphere also responds to solar variability, and could transfer these responses to layers below (Smith, 2012). In this way the mesosphere is controlling the interactions of the atmosphere and the near-Earth space environment.

Due to its short chemical lifetime (∼weeks), the mixing ratio of ozone is sensitive to environmental variations introduced by waves. Smith et al. (2018) found that changes in OH, H_2O quantity and temperature are contributing to interannual variations, as well as differences between the southern and northern hemisphere MMM. During winter, the downwelling of air inside the polar vortex might transport species from the upper mesosphere down into the lower mesosphere and stratosphere. Funke et al. (2005) documented that dynamically transported NO_x destroyed ozone in the stratosphere in this way. This form of dynamical transport is far from predictable, and depends on polar vortex stability and dynamical variability.

Mesospheric ozone depletion due to transported NO_x originating from the thermosphere is even less certain. Using WACCM model simulations of vertical transport of trace species from the thermosphere to the middle atmosphere, Smith et al. (2011) found a cell with reverse motion relative to the dominating downward motion of the high latitude winter mesosphere. The region of downward transport within the polar vortex was not found to extend into the thermosphere. A measurable reduction in mesospheric ozone due to downward transport of odd-nitrogen produced in the thermosphere by auroral particles is therefore questionable.

2.3 Space environment

The near-Earth space environment is far from empty vacuum; it is filled with energetic solar radiation and charged particles governed by magnetic forces. The Earth's magnetic field couples with the interplanetary magnetic field originating from the Sun, and in this way solar particles enter the upper and middle atmosphere. High-energy particles from the Sun and even cosmic rays may also travel directly through our protective magnetosphere and into the atmosphere. This section will deal with the processes of how the Sun's particles enter our atmosphere, what effects they might have and how we measure them. The following is mainly based on the books by Kivelson and Russel (1995) and Fitzpatrick (2014) and Prölss (2004).

2.3.1 The solar wind

The Sun's magnetic field is a very active field of study. We are able to observe the magnetic field at the corona as it governs the motion of the plasma, and magnetographs measure the strength and direction of the fields deeper in the photosphere, yet several questions remain open. Where exactly in the Sun does the magnetic field and solar wind originate? What generates them? What causes the eleven-year activity cycle? How does it affect our climate?

A constant stream of electrons and ions escape the Sun and travel radially away in all directions, its properties varying with magnetic activity, time and distance. This plasma is called the solar wind, and its entrained magnetic field is the interplanetary magnetic field (IMF). As the solar wind progresses through the solar system and encounters obstacles in its flow including magnetized and unmagnetized planetary bodies, its properties evolve.

The solar wind generally exists in one of two fundamental states; the slow solar wind or the fast solar wind. The fast solar wind originates from the polar regions of the Sun and coronal holes, with a composition similar to that of the photosphere. If the coronal hole is at lower latitudes, it can impact the Earth with high-speed streams (HSS) of solar winds, causing geomagnetic disturbances. The slow solar wind is associated with the so called streamer belt around the Sun's equatorial region (Feldman et al., 2005). It originates from the corona, as can be deduced from its composition.

Table 2 shows how the properties of the more common slow solar wind evolves with radial distance from the Sun. One would expect the particle densities to fall of by R^{-2} as for an even, radially expanding solar wind, but that is not the case, and so the density decreases slightly less steeply (Kivelson and Russel, 1995). The electron and proton densities are equal for the slow solar wind. The dynamic pressure follows the decline of the particle density. The temperature also decreases with radial distance, but less so than what would have been the case for an adiabatic process. This temperature behaviour might be due to heat conduction and dissipation, or conversion of bulk flow energy into thermal energy by stream interactions and shocks, as described by Ebert et al. (2009). According to Collard et al. (1982), the mean radial velocity of the solar wind remains largely unchanged from 1-15 AU.

Properties	Earth (1 AU)	Radial dependence
Velocity	400 km/s	∼constant
IMF	∼6 nT	$R^{-1.4}$
Electron density	7.1 /cm^3	$R^{-1.86}$
Proton density	6.6 /cm^3	$R^{-1.86}$
Temperature	1.5×10^5 K	$R^{-0.7}$
Dynamic pressure	5 nPa	$R^{-1.86}$

Table 2: Properties of the slow solar wind at 1 AU as well as the radial dependence of said properties (Ebert et al., 2009).

By the time the solar wind reaches the Earth, after approximately four days of supersonic travel, its density has declined drastically, but because of its energy (velocity remains constant) it could still be harmful to life on the surface. Without a global magnetic field, the Earth would probably have an environment much closer to that of Mars, where the atmosphere has been stripped away over millions of years by the continuously present solar wind. Our geomagnetic field deflects incoming particles, redirecting most past the planet, allowing life as we know it to evolve.

2.3.2 The magnetosphere and magnetic reconnection

The intrinsic magnetic field of the Earth has three sources: the internal magnetic field created by currents in the metallic liquid core of the Earth, local magnetic fields from remaining crust magnetization and magnetospheric and ionospheric currents inducing fields of their own. The latter two combine with the Earth's internally generated dipolar magnetic field to form the topology of the finite volume called the magnetosphere. The outer boundary of the magnetosphere is called the magnetopause. On the Sun-facing dayside, the magnetopause is at a distance of $\sim 10 R_E$, but under extreme conditions such as during solar storms it can be pushed in as close as $3R_E$ from the center of the planet. The location of the magnetopause is decided by hydrostatic equilibrium, equalizing the magnetic pressure in equation 2.12 and the kinetic pressure of the solar wind in equation 2.13.

$$P_{Earth} = \frac{B^2}{2\mu_0} \tag{2.12}$$

$$P_{SW} = \rho_{SW} \cdot v_{SW}^2 \tag{2.13}$$

In equation 2.12 B is the total (external and internal) magnetic field of the Earth and μ_0 is the vacuum permeability. In equation 2.13, ρ_{SW} is the particle density of the solar wind and v_{SW} is the velocity of the solar wind.

The Geocentric Solar Magnetospheric coordinate system is often used when discussing the magnetosphere. $\hat{x}$ is defined as pointing to the Sun along the Sun-Earth line, the xz plane contains the magnetic dipole with positive $\hat{z}$ chosen to point towards the northern magnetic pole and $\hat{y}$ follows from the right hand rule (figure 7 represents a cut in the xz plane). The magnetosphere can be roughly approximated by a dipole model, but it is shaped by the solar wind and a complex system of currents, molding it into a bullet-like

shape. The shape of the magnetosphere can be seen in figure 7, with its characteristic flattened dayside magnetopause and elongated tail region. The region separating field lines bending towards the dayside and the ones extending into the nightside is called the cusp region. Field lines in the cusp are open and connected to the IMF. It should be noted that the magnetosphere is not in a static equilibrium state. As the solar forcing varies on time scales of minutes, the magnetosphere is a highly dynamical environment under constant change. Even when the solar wind is quiet, instabilities may occur from variations in the intrinsic terrestrial magnetic field.

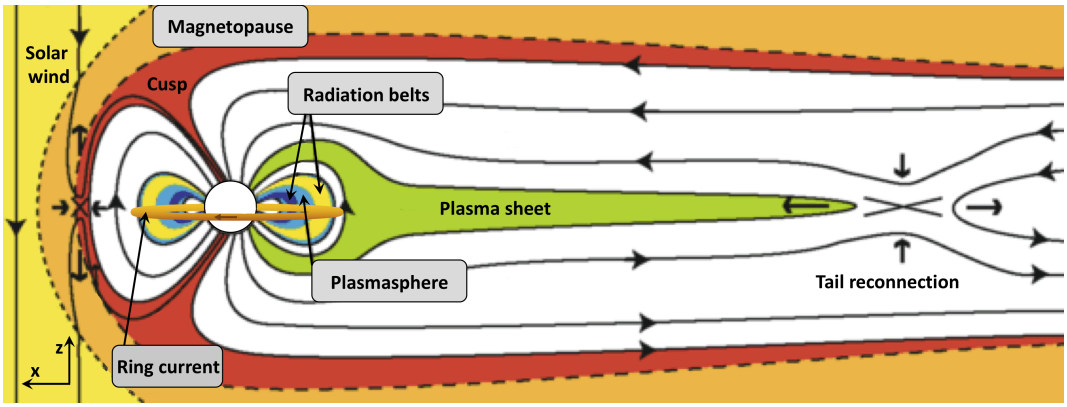

Figure 7: Model of the magnetosphere, showing the coupling of the IMF and the terrestrial magnetic field. Radiation belts, plasmasphere and ring current regions are labeled, as well as the cusp and tail regions. Coordinate system indicated in lower left corner, model with south pointing IMF. Figure adapted from Eastwood et al. (2015).

Particles in the magnetosphere originate from the upper atmosphere, ionosphere, the Sun and some are of cosmic origin. The most common way of solar particles entering our magnetospheric system is by magnetic reconnection which occurs regularly all along the magnetopause, but is generally divided into dayside and nightside reconnection. Reconnection enables the formation of open field lines, as seen in the cusp region, with one end attached to the Earth and the other connected to the IMF.

Magnetic reconnection occurs when the orientation of the z-components of the fields are anti-parallel. As the terrestrial magnetic field is static in its orientation (at least on time scales shorter than 400000 years), the IMF requires a south-pointing direction of its z-component ($B_z < 0$). When this is the case, the magnetosphere may transform from a closed system with dynamic boundaries, to an open system where particles and energy are transferred from the IMF into the terrestrial system.

Charged particles are kept within the magnetosphere, and are ordered in altitude according to their energies. When discussing distances from the Earth in space physics, the variable called the shell parameter (L) is often used. L labels the dipole field lines, and at the magnetic equator L corresponds to the radial distance from the center of the Earth to the given field line, in units of Earth radii. Its mathematical definition is:

$$L = r(\phi = 0)/R_E,$$

where ϕ is the geomagnetic latitude and R_E is the radius of the Earth. Given an L value, the field lines at this distance can be traced down to the Earth surface and the magnetic latitude of their footpoints can be calculated.

The three main areas of heightened particle density are the radiation belts, the ring current and the plasmasphere, but it is important to note that most of the ring current is carried by radiation belt particles, and all belt particles contribute to the ring current. The innermost region is the Van Allen radiation belts; two toruses containing highly energetic particles thought to mainly originate from cosmic rays and their decay processes, and the solar wind. The inner belt is located at L = 1.5, and is largely populated by energetic protons (10 - 100 MeV) originating from the solar wind. The inner belt is quite stable when it comes to magnitude and spatial extent, although the outer edge from L = 1.7 - 2.5 shows large temporal variability related to solar energetic proton events. The slot from L = 2 - 3 is mostly devoid of particles under quiet-time conditions, but can fill up with moderate to high energy particles during geomagnetic storms. The outer belt consists primarily of electrons (∼1 MeV), it is highly connected to storm time variability and typically extends from L = 3 - 6.5, although the spatial extent of the outer belt shows extreme variability. During solar minimum, the mean solar wind can be extremely low ($v_{SW} < 300\,\mathrm{km}$) for prolonged periods of time. When the solar wind velocity is this low, the outer belt can almost completely disappear (Baker et al., 2018), as happened during the solar minimum of 2008-2009.

Partially overlapping and extending further outward is the ring current. It contains protons and electrons like the Van Allen belts, but also some ionized atomic helium and oxygen. The energies are on the magnitude of ∼keV. Lastly, the plasmasphere overlaps with both the Van Allen belts and the ring current, and contains electrons and ions of very low energies. The ionosphere is the source of particles to the plasmasphere and to some extent the ring current. The ring current is also fed from the plasma sheet, which in turn contains particles inserted into the magnetosphere from the solar wind through tail reconnection.

During and immediately after reconnection, charged particles are accelerated towards the Earth within the plasma sheet, moving parallel to the geomagnetic field with a gyrating motion. As a particle moves toward the poles, the geomagnetic field strength increases and the particle velocity parallel to the field is reduced (the gyrating motion is unaffected). If the particle's pitch angle is small enough, it hits the atmosphere and is lost. If not, the particle is reflected and goes back up the guiding field line before being reflected again near the other pole, causing it to bounce back and forth between hemispheres. This trapping is called magnetic mirroring. In addition to the gyrating motion and mirroring, the trapped particles also revolve around the Earth, moving perpendicular to the geomagnetic field while remaining at the same distance from the Earth at all times. The electrons move in an eastward direction while the ions move westward, with a drift period ∼days. This drift initiates electric currents.

During long periods of southward IMF (∼hours), geomagnetic enhancements may develop gradually, or by sudden events such as coronal mass ejections or HSS blowing past the Earth. While B_Z is positive, sudden energetic event may cause no storm at all. Storms energize the radiation belts and ring current, causing a significant depression in the equatorial magnetic field. These perturbations are detected by the Dst index, and precipitating particles cause atmospheric phenomena such as the northern lights, and affects the chemistry in lower levels of the atmosphere.

2.3.3 Electric current systems

The terrestrial magnetosphere creates a cavity embedded in the solar wind. The magnetosphere is shaped by the equilibrium of the magnetic pressure of the Earth and the dynamic pressure of the solar wind (see equations 2.13 and 2.12), and complex system of external currents. The currents connect otherwise separate regions of the magnetosphere, and provide a bridge from the magnetosphere into the ionosphere for particles and energy to be exchanged. As stated by Potemra (1983), the geomagnetospheric system consists of five main features;

- a dayside current system perpendicular to the field
- tail currents,
- Birkeland currents parallel to the magnetic field flowing into and out of auroral regions,
- an ionospheric current system.

The amplitude of all these currents are closely linked to solar activity. There is no definite boundary between the atmosphere and outer space. Similarly, there is no clear boundary between the magnetosphere and the ionosphere. The partition is calculated to be where charged particles switch regimes from mainly being influenced by magnetic forces to mainly being controlled by collisions. This section will focus on the magnetospheric ring current and the auroral electrojets which are part of the ionospheric Hall current system.

Ring current
As described in the previous section, charged particles are injected into the plasma sheet by of magnetic reconnection. Electrons with energies $<$10 keV and protons with energies 1-200 keV are trapped in the Van Allen radiation belts by mirroring, where they produce an electric current by drifting around the planet. The ring current lies in the equatorial plane at a distance of $\sim 5R_E$. During geomagnetic storms, Earth's magnetic field is significantly decreased as large amounts of plasma is injected into the ring current region over the course of a few hours. The sudden injection causes a rapid increase in current magnitude while also shifting the current closer to the planet since the newly added particles are more energetic than the quiet-time ring current particles. The ring current induces a magnetic field opposite to the geomagnetic field, creating a corresponding decrease in the geomagnetic field. Some of the charged particles eventually precipitate out of the magnetosphere and down into the upper atmosphere at auroral and subauroral latitudes by scattering into the loss cone. The atmospheric changes due to particle precipitation will be discussed in section 2.4. The reduction in the Earth's magnetic field induced by the ring current is measured by the Dst index, described in section 3.3.2. The Dst index is a good measure of the number of charged particles contained in the inner magnetosphere (in both radiation belts) (Fitzpatrick, 2014).

Auroral electrojets
Electrojets are intense horizontal currents in the ionospheric E-region at altitudes of about

120 km. There are several electrojet systems; equatorial electrojets, partial nightside electrojets and auroral electrojets. Here we focus on the auroral electrojets, which flow westward and eastward within the polar oval, as visualized in figure 8. The auroral electrojets are part of the Hall current system which corresponds to the plasma convection in the polar region. Due to the difference in drift velocity between electrons and ions (ions are slower), the current runs anti-parallel to the flow motion.

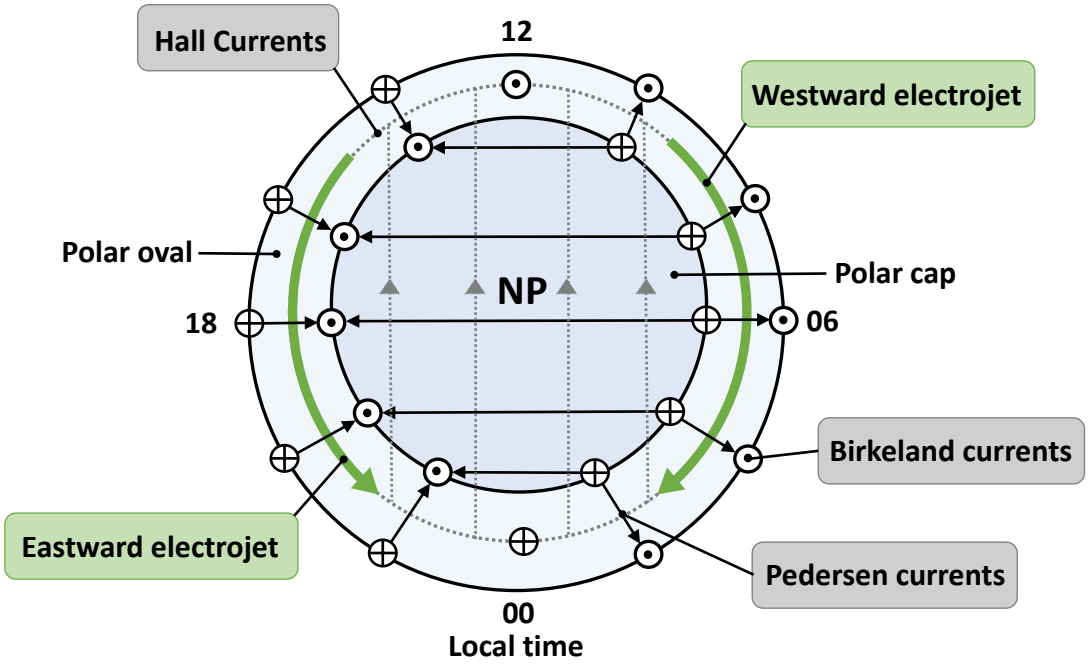

Figure 8: Current systems in the polar ionosphere. Hall currents (Birkeland and Pedersen), as well as eastward and westward auroral electrojets. The polar oval and the polar cap is indicated. NP denotes the magnetic north pole.

Within the polar cap the Hall current flows towards the Sun. When the edge of the cap is reached, the ions travel azimuthally west, and the electrons travel azimuthally east. These two azimuthal currents are the dawn-side westward and a dusk-side eastward components of the auroral electrojet. The jets are measured by twelve ground magnetometers at auroral latitudes. These measurements form the basis for the geomagnetic AE index described in section 3.3.1. Similar to the ring current, the auroral electrojet also induces a magnetic field which reduces the geomagnetic field measured on the surface.

2.4 Energetic particle precipitation

Energetic particle precipitation (EPP) is an expression for highly energetic protons, electrons, neutrons and ions that enter the atmosphere. The particles can be of solar, magnetospheric origin or cosmic origin. Particles precipitate into the atmosphere from different regions of the magnetosphere, driven by solar wind conditions and geomagnetic processes. The following section focuses on charged solar and magnetospheric particles.

Figure 9 shows the penetration depth of different charged particles as a function of initial energy.

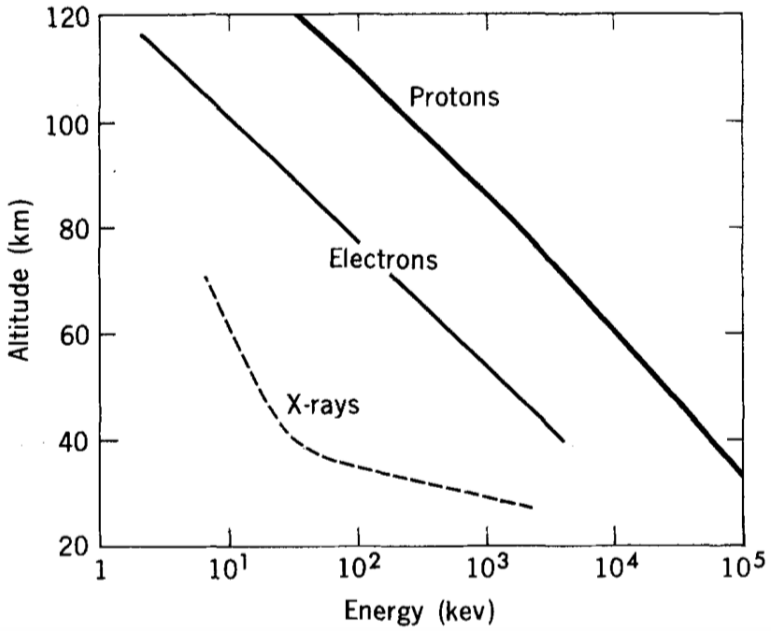

Figure 9: Penetration depth of electrons and protons vertically incident on the top of the atmosphere as a function of energy. Figure from Thorne (1980).

We distinguish between solar energetic particles (SEP), radiation belt particles (RBP) and auroral particles (AP). They differ in origin, particle energy and subsequently precipitation latitude. Figure 10 shows the different categories of energetic particles and at what altitudes they predominantly ionize atmospheric constituents.

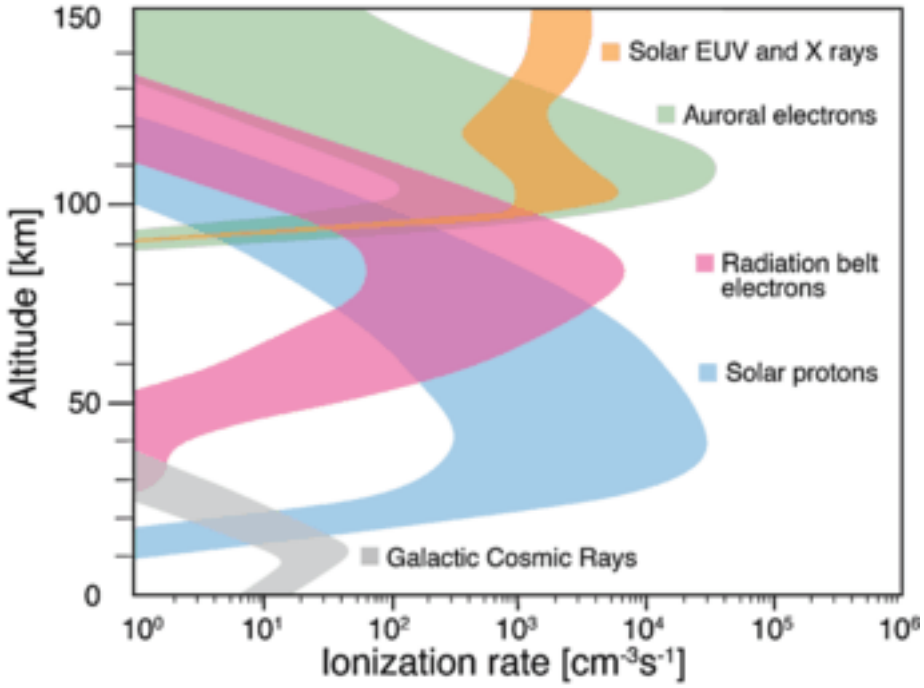

Figure 10: Ionization rates from solar radiation and energetic particles. Figure from Mironova et al. (2015).

SEP are dominated by protons, and are associated with fast, violent energy-burst phenomena on the Sun such as solar proton events, coronal mass ejections and solar flares. The particles have energies up to several hundred MeV, and can cause cascade events in the atmosphere leading to the productions of muons detectable from ground. SEP mostly precipitate directly down on open magnetic field lines coupled to the IMF and enter the atmosphere at high latitudes in the cusp and polar cap regions.

RBP originate, as the name implies, from the Van Allen radiation belts (see 2.3.2), they are of medium energy at ∼MeV (compared to SEP and AP) and are contributing to the ring current by revolving around the Earth at L = ∼5. The field lines here are closed and have footpoints at auroral latitudes and below, making the precipitating area of RBP between $80-30°$.

AP consist mostly of low-energy electrons (∼keV). The low energy is an indication of their origin in the plasma sheet; a region just beyond the radiation belts (L=∼7). At this distance, the guiding field lines have footpoints at latitudes within the auroral oval, usually positioned between $60-80°$. The position and shape of the oval is dynamic and highly responsive to solar and geomagnetic forcing. Precipitation occurs on both day and nightside.

Auroral and radiation belt particles overlap to a great extent when it comes to precipitation area, although radiation belt particles can also precipitate to slightly lower latitudes than what auroral particles are capable of. AP and RBP also overlap slightly in ionizing altitude (overlap region from $90-130$ km). RBP peaks at 80 km, while AP peaks at 110 km (see figure 10).

2.4.1 Effects of EPP

During geomagnetically disturbed periods, the upper atmosphere experiences enhanced energy transfers from space from Joule heating and particle precipitation. The incoming particles affect the chemical composition of the atmosphere by ionization, excitation and dissociation.

Energy and mass dictate how deep the charged solar particles penetrate into the atmosphere. As the particles travel through the atmosphere they ionize and dissociate neutral species (e.g. O_2 and N_2), leading to production of reactive species NO_x and HO_x (Barth, 1992). Near the mesopause, where there is H instead of water vapour due to photodissociation, the EPP ionization processes end up producing OH^*-ions which de-excite and create air glow. At lower altitudes, where the concentration of water vapour is significant, EPP produces OH in the ground state, which does not create air glow, but instead takes part in catalytic cycles involving O_3.

The impact of EPP, and subsequently NO_x and HO_x, on the neutral atmosphere depends on the chemical lifetime of the catalytic species. We therefore differentiate between direct effects (EPP-DE) and indirect effects (EPP-IE). EPP-DE means highly localized atmospheric responses in space and time, while EPP-IE are long lasting effect, or effects caused by the reactive species after transport to a region outside their production area. The short-lived HO_x ($\sim$hours) only partakes in EPP-DE, while NO_x can be carried along with winds, or be transported from the thermosphere and mesosphere to other altitude regions by downward circulation during polar winters (Randall et al., 2009). Figure 11 shows an overview of where direct and indirect EPP effects take place. In the absence of sunlight during polar night, the lifetime of mesospheric NO_x can be several days, which may cause NO_x to be moved both horizontally and vertically. Downward transport during the polar winter increases the lifetime of NO_x even further, enabling the species to be transported large distances. The average velocity of the molecules within the polar vortex is $\sim$4 km/day of downward motion.

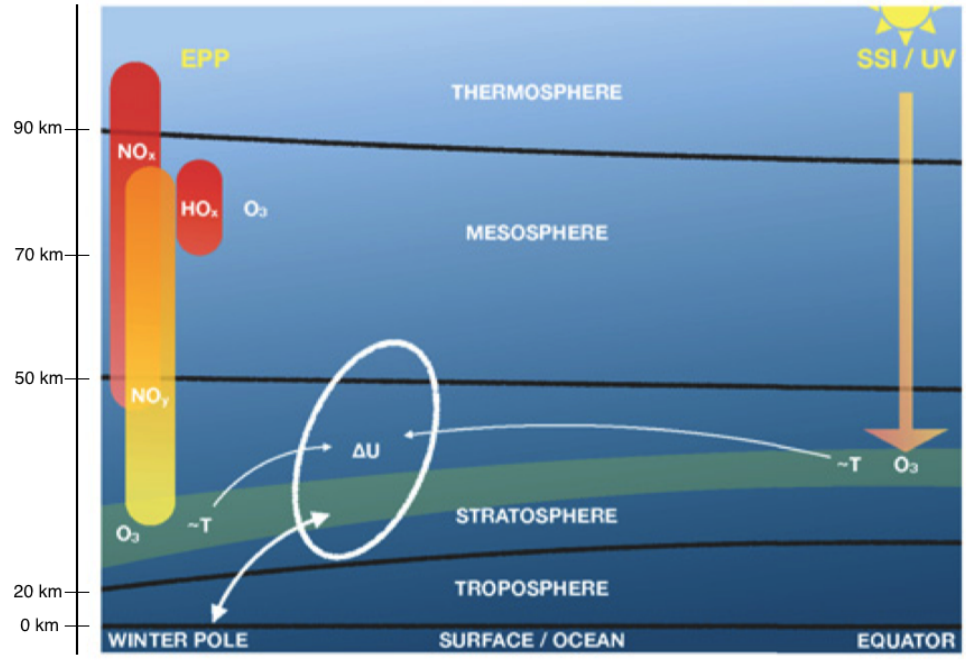

Figure 11: Solar forcing on middle atmosphere. Red bars represent effects by direct production of NO_x and HO_x while the yellow bar represents transported NO_y. Thin white lines show temperature variations interacting with zonal winds (U). Gravity wave filtering (thick white line) changes with winds. Figure modified from Hendrickx (2018).

When NO_x is transported to lower altitudes, it becomes part of a reactive nitrogen group NO_y ($NO_y = NO_x + HNO_3 + HNO_4 + ClONO_2 + BrONO_2 + 2\,N_2O_5$) (Sinnhuber et al., 2012). Where NO_x, NO_y and HO_x affect the neutral constituents of the atmosphere is showed in figure 11. In polar mesospheric and lower thermospheric (MLT) regions, Hendrickx et al. (2017) found that geomagnetic activity is the dominant process for short-term NO changes. NO_y is found to increase at altitudes where EPP does not reach in polar regions during winter, indicating the increase is due to transported nitrogen species with long lifetimes. Rohen et al. (2005) reported two distinguishable regimes of middle atmospheric ozone loss; ozone loss below 50 km was driven by NO_x, while ozone loss above 50 km was driven by the HO_x cycle, each with a different ozone depletion and recovery time evolution.

The MMM peaks at ∼70 km, where solar protons and radiation belt/ring current electrons dominate the ionizing landscape (see figure 10). EPP-DE can occur by the production of both NO_x and HO_x. Due to the low density of HO_x near the polar night terminator, a moderate to major precipitation event may produce amounts of HO_x comparable to, and even exceeding, what is produced naturally during the day (Sofieva et al., 2009). For auroral electrons to play any part in the middle mesospheric ozone budget, they need to come by indirect effects; NO_x created at ∼90 km and transported down. For this EPP-IE we would expect to see an ozone response after ∼4-5 days.

3 Instruments

3.1 British Antarctic Survey Microwave Radiometer at Troll

Ozone, pressure, altitude and temperature profiles from 2008-2009 were provided by the British Antarctic Survey's ground-based Microwave Radiometer at Troll station (BAS-MRT), Antarctica. At 72° south and 2° east (62° Mlat), the instrument is located well within the southern auroral oval, as the poleward boundary seems to be stationary at 72° Mlat and the equatorward boundary moves according to the magnetic activity (Xiong et al., 2014). The instrument was operational at Troll from February 2008 through January 2010, retrieving ozone profiles approximately every hour. For more details about the instrumentation and data retrieval, see Daae et al. (2013).

BAS-MRT measured the spectral regions around the rotational transitions of NO at 250.796 GHz, CO at 230.538 GHz and O_3 at 249.96 GHz. The ozone line corresponds to emissions of wavelength 1199.36 µm. The a priori for the temperature and O3 profiles are taken from the Whole Atmosphere Community Climate Model with Specified Dynamics (SD-WACCM). The temperatures are adjusted partly by the optimal estimation retrieval procedure in Daae et al. (2013). The retrieval of the O_3 spectra resulted in 13 648 profiles covering 675 days with an average of about 20 profiles per day, with each spectra integrated for one hour to increase the signal-to-noise ratio.

In this study we focus on the altitudes around 70 km. Daae et al. (2013) shows that the tertiary ozone maximum is captured with a measurement response of at least 0.8 up to 72 km. the The a priori influence becomes more significant with altitude, but the measurement response is still least 0.5 up to 76 km. The vertical resolution in this region is close to 17 km (Kleinknecht, 2015).

3.2 EOS Aura Microwave Limb Sounder

The Earth Observing System (EOS) Aura satellite was launched by the National Aeronautics and Space Administration (NASA) in 2004. Aura's mission objective is to measure atmospheric composition, temperature, humidity and ice clouds for the purpose of tracking the stratospheric ozone layer, to improve predictions of climate change and humanity's understanding of air quality. In this thesis, EOS Aura provides ozone, temperature and geopotential height profiles for 2010.

Aura orbits the Earth close to 15 times a day in a near-polar sun-synchronous orbit at an altitude of 705 km. The Microwave Limb Sounder (MLS) is one of four instruments on board Aura, and it observes thermal microwave emissions from the edge of the atmosphere, called limb, and scans from the ground to ∼90 km every 25 seconds. MLS uses several heterodyne radiometers for its measurements; the one optimized for O_3 observation is centered on 240 GHz, where a strong ozone line is within a spectral range where absorption

by water vapour is weak. Retrieved MLS Level 2 (v3.3) data of Aura are in HDF-EOS version 5 format.

For this project, ozone, temperature, pressure and geopotential height profiles are chosen if they satisfy the *quality*, *precision*, *status* and *convergence* conditions described by (Livesey et al., 2011). Furthermore, profiles were only used in the analysis if they are within a 5×5° lat-lon grid centered around Troll station, with a solar zenith angle larger than 100°. Geometric height (altitude) is converted from the provided geopotential height profiles.

Based on the averaging kernels in Livesey et al. (2011), the vertical resolution for MLS in the mesosphere is $4-6$ km, with datapoint information dominated by measurements all the way up to 0.02 hPa (~ 72 km). The horizontal resolution is 200 km.

3.3 Geomagnetic indices

Geomagnetic indices have long been used to detect and quantify geomagnetic storms in the magnetosphere. The indices aim to describe the geomagnetic activity, or some of its components. Each of them is related to a phenomenon in the magnetosphere or ionosphere, but the spatial and temporal coverages vary between the indices.

Today the International Association of Geomagnetism and Aeronomy officially endorses several different indices, among them the Auroral Electrojet (AE), Disturbance storm time (Dst) and the "Planetarische Kennziffer" (Kp) and the Polar Cap indices (PC-north and PC-south) (Data Analysis Center for Geomagnetism and Space Magnetism, 2015). In this study the AE and Dst are utilized to cover the precipitation of both auroral and radiation belt particles. The data was provided by the World Data Center for Geomagnetism, Kyoto.

3.3.1 AE index

Auroral Electrojet data dates back to 1957, and the index was officially introduced by Davis and Sugiura (1966). The AE index is not a direct measure of a physical quantity, but is calculated in such a way that it ideally is the total deviation from quiet day values of the horizontal H-component of the geomagnetic field at auroral latitudes.

Twelve observatories in the Northern hemisphere constantly measures the H component of the geomagnetic field. The observatories are distributed as evenly as possible in longitude at auroral latitudes, with one instruments in Sweden, Greenland (Denmark) and Iceland, two in the United States of America, three in Canada and four in Russia. The index has a temporal resolution of 1 min with a unit of nT, although most available datasets are hourly averages. As of today, no similar coverage exists in the Southern hemisphere, but previous studies have shown good correlations between conjugate ground magnetometers although the difference in magnitude is significant with the southern hemisphere showing weaker activity.

The index is defined as the difference between the auroral electrojet upper (AU) and lower (AL) indices;

$$AE = AU - AL.$$

AU and AL express the strongest current intensity of the eastward and westward auroral electrojets, respectively (see figure 8). The AO index is defined as the average of the

AU and AL indices and represents a zonal mean of the current system. The AE index represents the overall activity of the electrojets. The term "AE indices" usually represents all four indices (AU, AL, AE and AO) (Data Analysis Center for Geomagnetism and Space Magnetism, 2015).

3.3.2 Dst index

The Disturbance storm-time index is derived by a network of four geomagnetic observatories near the equator. The locations were chosen on the basis of measurement quality, sufficient distance from both auroral and equatorial electrojets and an even distribution in longitude. Data is available all the way back to 1957, the temporal resolution is 1 h, and the index is expressed in nano teslas.

Measurements are mainly of the ring current intensity, but the tail current and the magnetopause Chapman-Ferraro current also influence the data as they are all in the equatorial plane. The index is corrected by removing contributions from the latter ones at each observatory. The Dst index is found by calculating the difference in the solar quiet time and the horizontal component of the terrestrial magnetic field (H). This is done for each observatory individually, before the hourly Dst for each observatory is averaged and normalized with respect to the dipole equator. The solar quiet time is found by averaging the five most quiet days of the month. Negative Dst indicates an enhanced ring current, which induces a magnetic field directly opposite to the Earth's magnetic field. The induced field weakens the geomagnetic field and reduces the H measured on the surface at equatorial and mid-latitudes. The strength of the horizontal component on the surface is inversely proportional to the energy content of the ring current, the magnitude of the decrease in H therefore represents the severity of disturbance. Positive variations in Dst are mostly caused by the compression of the magnetosphere from increases in the solar wind pressure.

4 Analysis

The data analysis for this project was done for the three Antarctic winter seasons of 2008, 2009 and 2010. BAS-MRT covered 2008 and 2009, but the number of storms during this period was insufficient for a satisfying superposed epoch analysis, therefore satellite data was included to extend the ozone measurements. EOS Aura was chosen because of its suitable orbit, and a previous study by Daae et al. (2013) which showed no significant bias when comparing BAS-MRT to MLS data. The ozone and geomagnetic index data was collected for the winter seasons of 2008, 2009 and 2010 between March 9th and October 21st of each year, a period of 227 days. Geomagnetic storms were selected from March 15th to October 15th of each year, as some quiet days before and after the storms were required for the superposed epoch analysis. Before mid-March and after mid-October ozone levels are generally too low for a successful superposed epoch analysis. Of the 13648 profiles retrieved from BAS-MRT, 4875 were both within the time intervals mentioned above and met the requirement SZA>100 degree. From EOS Aura/MLS, 157 profiles met all physical and instrumental requirements. While BAS-MRT gives evenly spaced hourly profiles (with the odd period of missing measurements due to instrumental down time), MLS has a poorer time resolution and provides slightly unevenly distributed profiles. Some days have two profiles only a few minutes apart, other days have two profiles several hours apart. Most days only have one profile, and a few days lack profiles altogether. In the cases where two profiles exists within the same our, the profiles are averaged so that the time resolution of one profile per hour is kept.

4.1 Ozone data

The two instruments providing ozone profiles differ in vertical resolution and number of datapoints in the mesosphere. In order to best compare the datasets, the profiles from MLS were interpolated to a vertical grid of altitudes matching those of BAS-MRT using cubic spline, before being smoothed using a weighted triangle.

The vertical distribution of datapoints in the MLS profiles is on a grid $\sim$5 km apart in the mesosphere, while the profiles from BAS-MRT have $\sim$2.2 km between grid-points. BAS-MRT has a vertical resolution of $\sim$17 km in the middle mesosphere and MLS has a resolution of about a third of that. A three point smoothing was applied to the MLS profiles, so that they approximate the resolution of the ground-based instrument.

For scientific use, Livesey et al. (2011) advises not to utilize datapoints at pressures at or lower than 0.01 hPa for MLS. Adhering to that recommendation would have limited this study to an altitude of $\sim$72 km, which is often at the center of the MMM. It was therefore deemed necessary to include the datapoint at 0.01 hPa, allowing entries closer to the deep minimum between the tertiary maximum and secondary layer to be included.

The pressure limit suggested by Livesey et al. (2011) is very cautious, and most datapoints added by allowing entries at 0.01 hPa pass all requirements. The few which do not are instead found by pchip extrapolation. Spline extrapolation was found to drastically

overestimate some values due to its purpose of creating a continuous result, while pchip has no overshoots and less oscillations. For the interpolation of the entire profile, spline was found to produce profiles most resembling the profiles of BAS-MRT.

Even though most datapoints at 0.01 hPa pass all *quality*, *precision*, *status* and *convergence* tests, some (as well as some of the extrapolated values) were wildly out of range of what is physically plausible. A limit set to ±3.5 ppmv was used to remove these entries, which were then replaced by the average value of all entries at the same altitude level.

As instruments reach the limit of their capacity of measurements in altitude, some weigh the a priori heavily. When later taking a time average of the profiles, this method results in the time average of the a priori. Other retrieval methods leave the extremely noisy entries in the data, so that when the profiles are time averaged, they end up as a climatology average. The latter approach is approximated in this study by replacing the extremely noisy entries with an average of the noise.

Figure 12 shows a selection of ozone profiles in the altitude region 10 −75 km from BAS-MRT compared to MLS before and after processing. Left panel shows profiles from BAS-MRT, only filtered with respect to SZA. The middle panel shows the MLS profiles without any processing, other than filtering out profiles not fulfilling the quality and SZA requirements. The right panel shows the same profiles as the middle panel, after extrapolation, interpolation and smoothing.

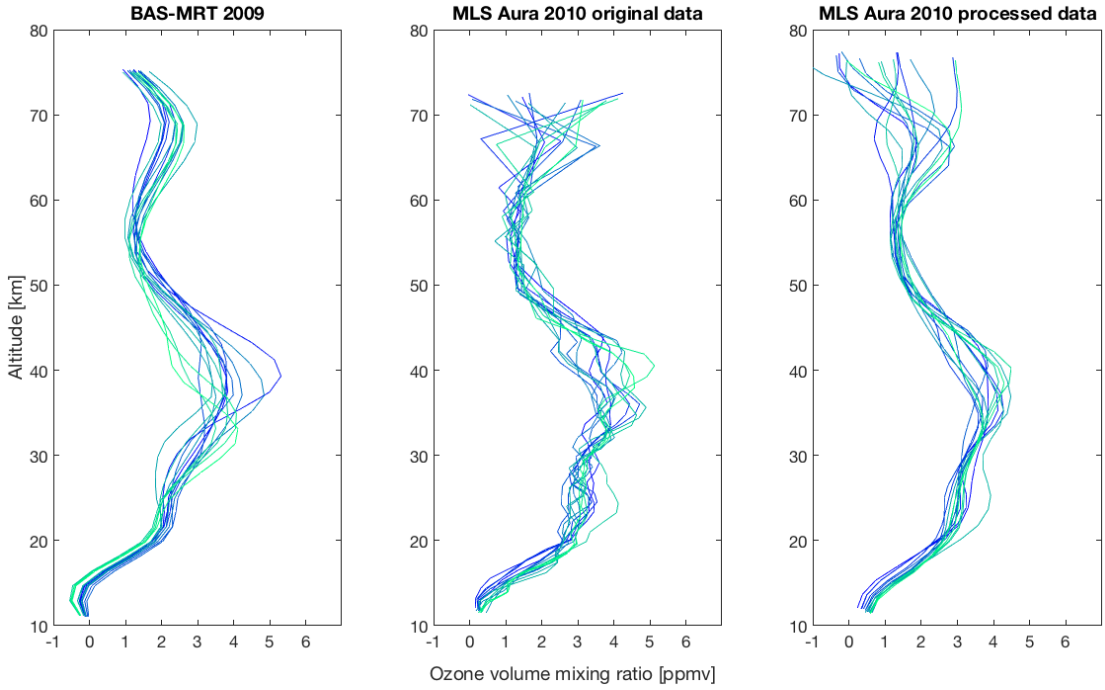

Figure 12: A selection of ozone profiles from May 15th to June 15th, for 2009 and 2010. The left panel shows measurements by the ground-based instrument, middle and right panel are from satellite measurements. The middle panel shows the original profiles, while the right panel shows the same profiles after processing.

Both instruments clearly confirmed the primary ozone layer and the ozone deprived region from 50 −60 km. BAS-MRT shows a significant and smooth tertiary maximum peaking at ∼68 km, reaching values up to 3 ppmv. The tertiary maximum is clearly

visible in the MLS profiles as well, although slightly less uniform in shape. One should keep in mind that the last data points in the MLS data were pushed slightly beyond the advised instrument limit, that the uncertainty of the last data points is 1.4 ppmv, and that some of the upper data points in the MLS data were extrapolated. The uncertainties for the entire ozone profile for the ground-based instrument as well as the satellite can be seen in figure 13.

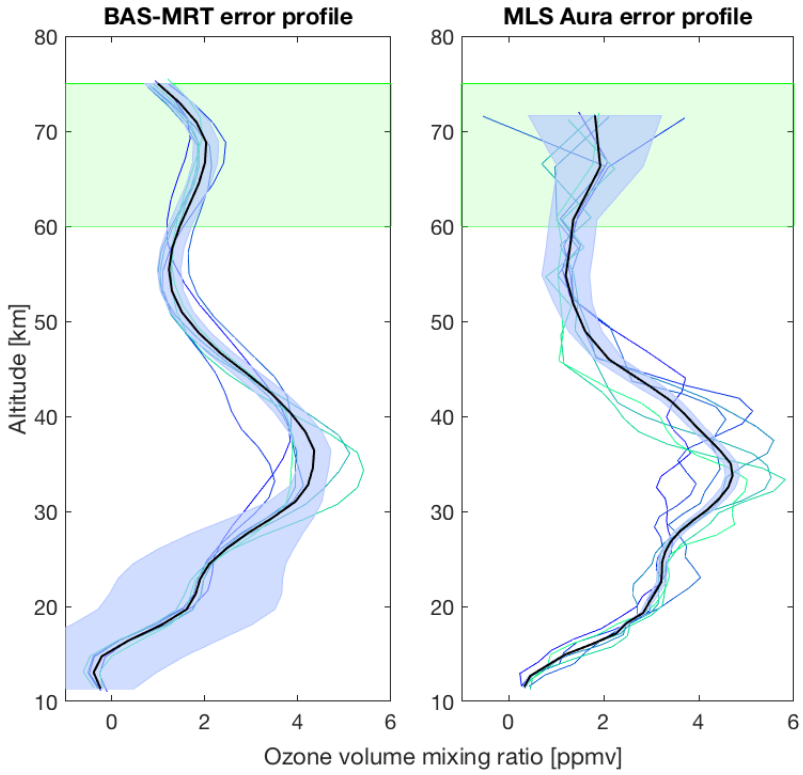

Figure 13: A selection of ozone profiles from May 1st to August 31st, for 2009 and 2010. The left panel shows measurements by the ground-based instrument, the right panel shows profiles from satellite measurements. The thick black line is the mean profile for the entire winter season and the blue shaded area indicates the uncertainty of the measurements as a function of altitude. The shaded green area highlights the altitude region of the middle mesospheric maximum.

The ground-based radiometer measures the lower/middle mesosphere with an error of < 0.3 ppmv. The measurements below 36 km are dominated by a priori and therefore less reliable. The satellite measures the lower/middle atmosphere most accurately, a result of the limb scanning method. The errors for the lower atmosphere are <0.2 ppmv. MLS measures most of the MMM with an uncertainty <0.9 ppmv. The last datapoint used in the profile reached an uncertainty of 1.4 ppmv.

The annual variations in the MMM are marked by an asymmetry with highest values around May, and a second but smaller maximum in August, as can be seen in figure 14. The general behaviour of the two maximums are because the instruments are measuring the MMM in one specific location (around the ground-based instrument), while the MMM moves with the season to stay near the polar night terminator.

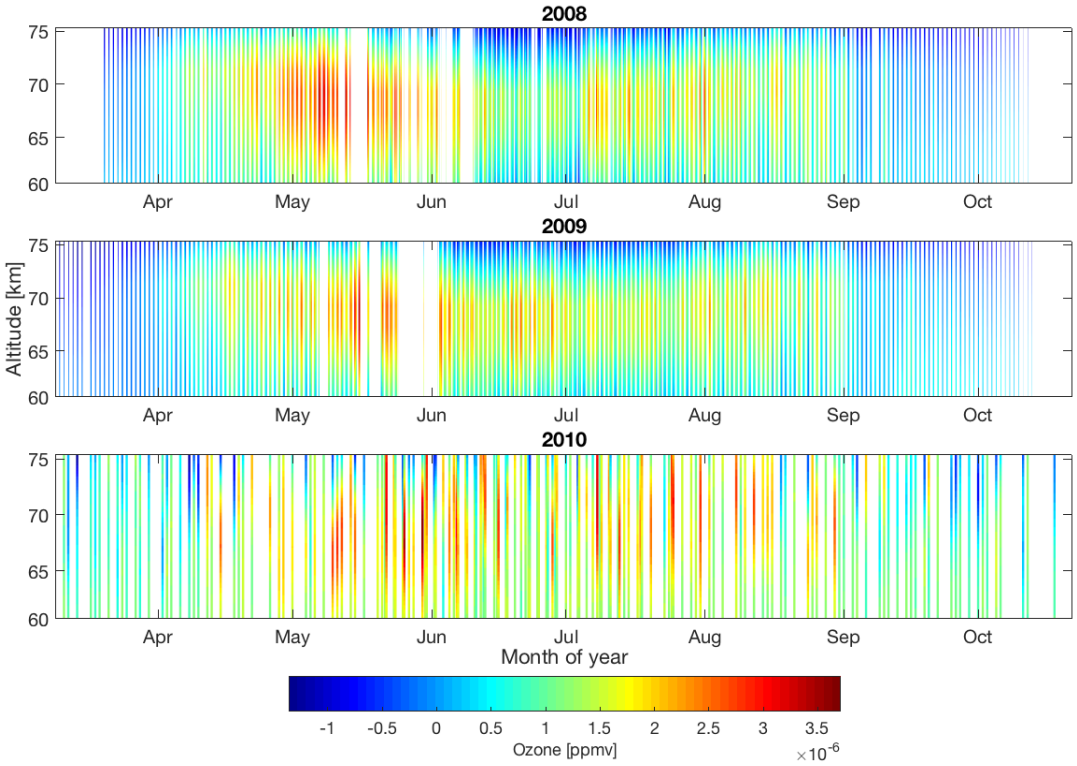

Figure 14: Nighttime ozone volume mixing ratios for winter seasons 2008, 2009 and 2010. Ticks at the 1st of each month. White spaces due to the removal of daytime profiles and instrument downtime.

The three years examined in this thesis differ slightly in seasonal ozone magnitude, peak altitude, and at what times the characteristic double-hump occurs. 2009 stands out with a slower build up of the first maximum, an increase in the end of June not seen in the other two years, and the second peak is almost non-existent. Oscillations can be seen leading up to the first maximum and following the second maximum, confirming the large day-night variations described in Sonnemann et al. (2007), even though figure 14 only shows profiles where SZA $> 100°$ ($10°$ below the horizon). The monthly ticks are at the first of each month, at midnight (or the profile closest to midnight). For 2008 and 2010 the double-hump appears as theory predicts (see section 2.2), in mid-May and then again in August.

Ozone column density

All ozone profiles were converted from volume mixing ratios (ppmv) to number density (m^{-3}), before being integrated over the altitude interval $60-75$ km. This altitude region covers the middle entire mesospheric maximum, from the deep minimum below to the minimum above. After integration over this interval, partial column density values (m^{-2}) are obtained.

Geomagnetic storms are identified from March 15th to October 15th of each year. During this period, the background ozone partial column values vary from $3 \times 10^{16}\,m^{-2}$ to $5.5 \times 10^{16}\,m^{-2}$. In order to compare the ozone responses to storms happening any time during the winter season, the ozone values were normalized with respect to climate vari-

ations. This was done by creating a seasonal background profile for each year, illustrated in figure 15, where they are plotted on top of the non-smoothed partial columns for each year.

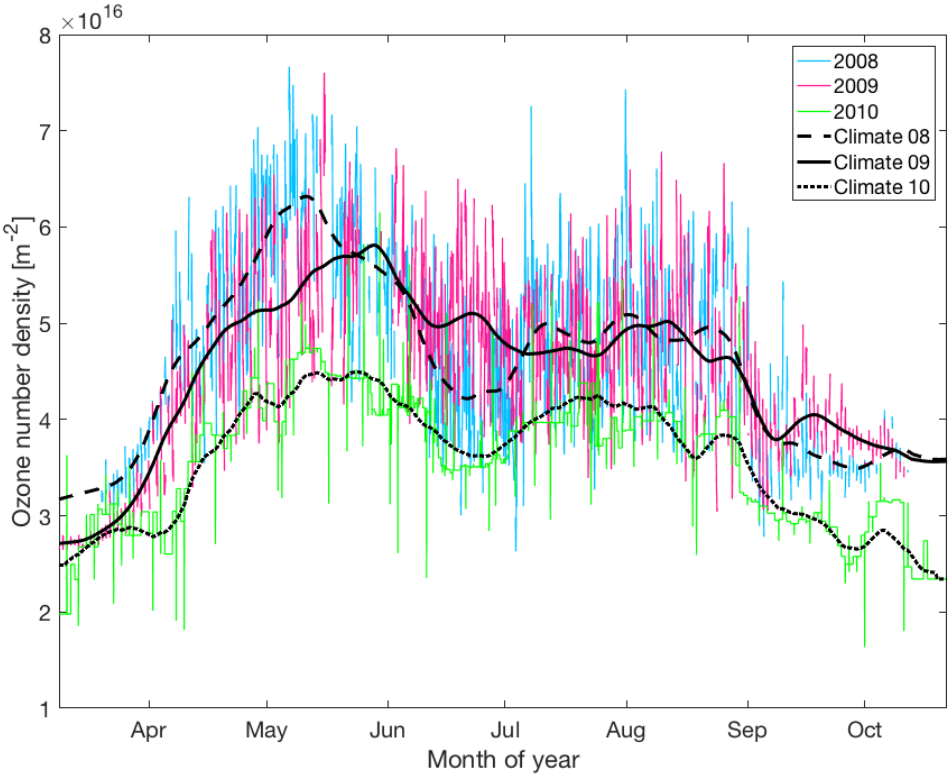

Figure 15: Ozone partial columns between $60 - 75$ km. The black line represents the averaged and smoothed ozone from the individual years, yielding the background ozone level.

The datapoints for 2010 are few compared to the two previous years (because of the ∼24 hour time resolution of MLS Aura) so to get a better visualization in this figure the profile is filled in using a moving median of 10 days.

The climatology for the individual years are calculated by applying a 10-day moving average twice, to the hour-by-hour partial columns. The moving average is a technique designed to smooth out short-term fluctuations and enhance longer-term cycles. These background profiles were used to reduce seasonal variability by subtracting them from the ozone time series, such that an unperturbed ozone value ideally is zero.

As seen in figure 15, the ozone levels for 2008 and 2009 are very similar to each other, while the ozone lever during 2010 is consistently ∼30% lower than the two previous years. The reason for the large difference might be an increase in solar activity since in 2010 the solar cycle began to recover from the extreme minimum in 2008-2009. Other factors like transport and annual variations of water vapour, affecting the production of odd-hydrogen and therefore ozone, might also have played a role.

4.2 Geomagnetic index data

Time series of AE and Dst indices were collected from the International Services of Geomagnetic Indices (2013) and the Data Analysis Center for Geomagnetism and Space Magnetism (2015). The three years chosen for this work were centered on the solar minimum between Solar Cycle 23 and Solar Cycle 24. Both indices during the Antarctic winter season of all three years are depicted in figures 16 to 18. The solar minimum from mid-2007 to mid-2009 had a record number of days without any sun spots, although there were periods of enhanced energy flow into the terrestrial atmosphere occurring periodically due to coronal holes (Gibson et al., 2009). Coronal holes are most often created during the declining phase of the Solar Cycle at the Sun's polar regions. The holes can migrate to mid-latitudes, and sometimes individual low-latitude holes appear. During the aforementioned solar minimum, several low-latitude coronal holes were observed, providing sources of solar wind high-speed streams (HSS) blowing past the Earth. The HSS may return with each solar rotation (27 days) as long as the low-latitude coronal holes persist, as shown in figure 16. The presence of multiple HSS can overcome the effects of a global decrease in the IMF, and could even counter the effects of reduced magnetic activity at the Sun.

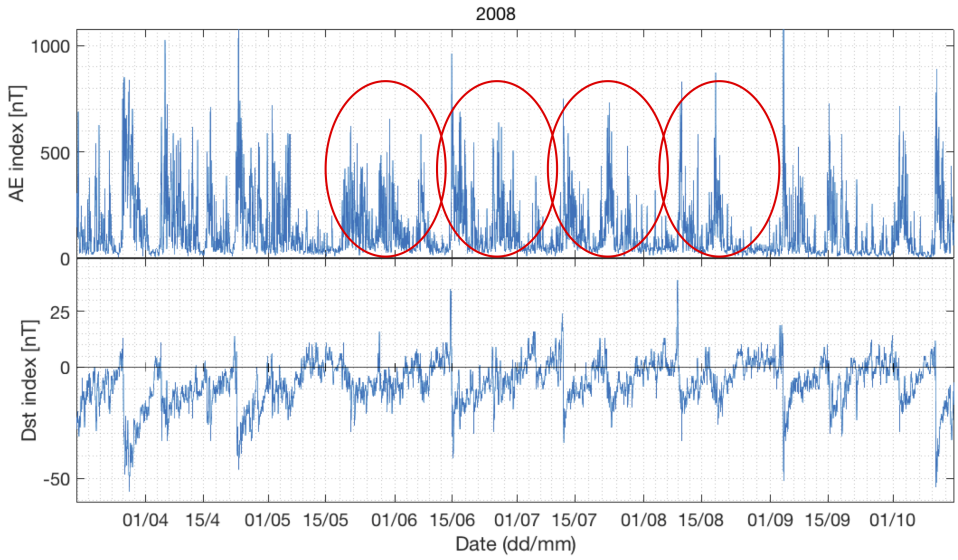

Figure 16: Geomagnetic indices AE and Dst from March 15th to October 15th 2008. A group of low-latitude coronal holes can be seen evolving in time within the red circles, appearing every 27th day over the course of three months.

Coronal holes occur when the Sun's magnetic field lines are open, allowing solar particles to escape with a larger velocity than the average solar wind. If a hole appears near the center of the disk of the Sun facing the Earth, we will detect an increase in geomagnetic activity with periodic cycle equal to the Sun's rotational period.

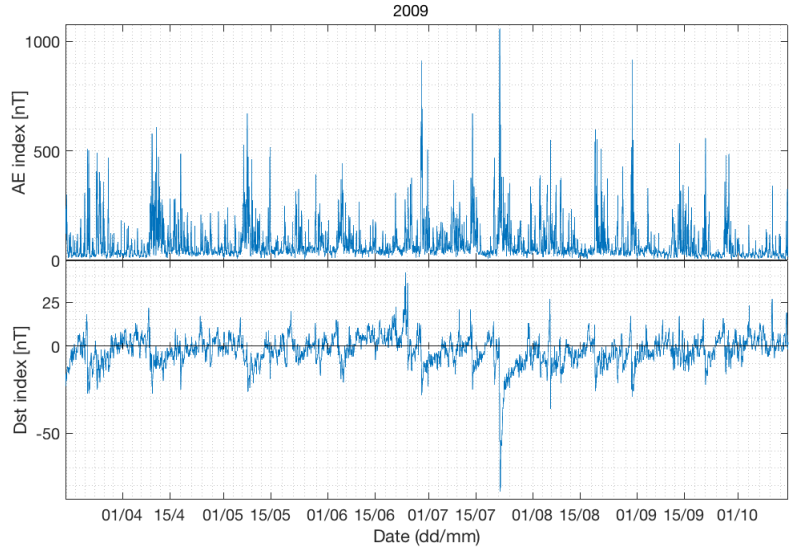

Figure 17: Geomagnetic indices AE and Dst from March 15th to October 15th 2009. Two spikes 27 days apart in April/May confirmed by Philips (2009) to be a coronal hole releasing high speed streams impacting on the Earth twice before fading.

2009 was the quietest year of the three used in this study, with only one storm reaching below $-50\,\mathrm{nT}$ on the Dst scale, which reached Earth on the 22nd of July, and was caused by a massive coronal mass ejection. A coronal hole can be seen disturbing the AE index twice in May/April, without any large depression of the Dst index.

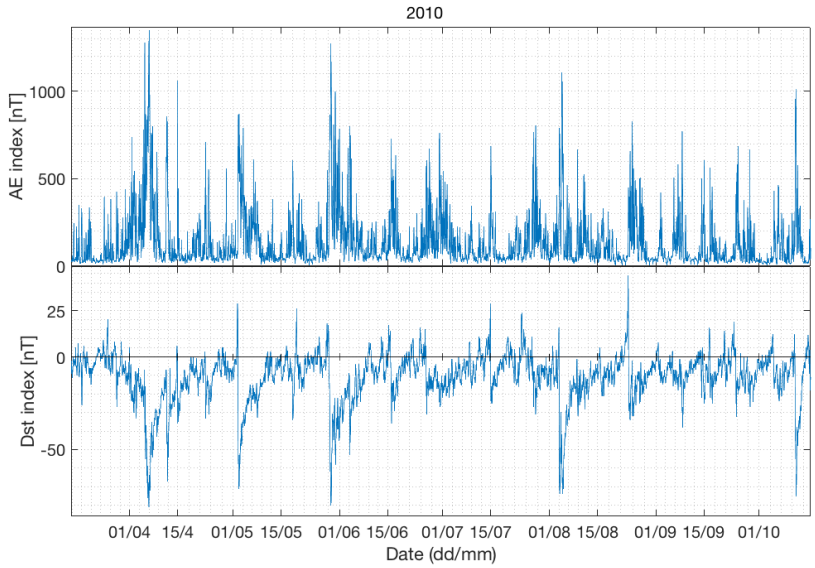

Figure 18: Geomagnetic indices AE and Dst from March 15th to October 15th 2010.

Solar cycle 24 began in 2010 with many moderate to extreme storms occurring in a short period of time. The high frequency of particle injection into the terrestrial magnetosphere may be the cause of the subdued levels of ozone in the MMM during the winter season of 2010 (see figure 14).

5 Results

In this thesis, two different methods to study the relationship between particle precipitation and ozone were utilized; a superposed epoch analysis and a cross-correlation analysis.

Superposed epoch analysis (SEA) is a non-parametric method used to test the statistical significance of extreme events and their forcing on other factors. It is a useful and widely utilized technique for isolating low amplitude signals that are otherwise obscured by background variability. Through the process of averaging key events, the stochastic background variability may be reduced enough such that low-amplitude signals become detectable.

The particle data is derived from geomagnetic indices, namely the AE and Dst. These are both sampled every hour. The ozone values is a time series of data sampled every hour from ground for 2008-2009, while 2010 is covered by satellite data with a time resolution of 1-2 days. Geomagnetic storms, typically referred to as "key dates", are selected based on physical criteria, which in this case will be the storm strength as measured by the Dst and AE indices respectively. The cross correlation is performed on these constructed superposed epochs, between ozone response and index data. Cross-correlation analysis is a tool meant to measure the similarity between two signals, in this case time series of ozone and a geomagnetic index.

5.1 Case study of a single storm

The initial phase of this thesis focused on individual storms that were measured by both the AE and Dst indices. Time series of these storms were visually compared to contour maps of ozone volume mixing ratio as well as ozone partial columns. Several individual storms were analyzed to understand the general behaviour of the indices during storms and the response of the middle mesospheric maximum, both in magnitude and in time. The storm discussed here originates from a coronal mass ejection impacting the Earth on the 22nd of July 2009. The storm is visualized by both AE and Dst indices in figure 19.

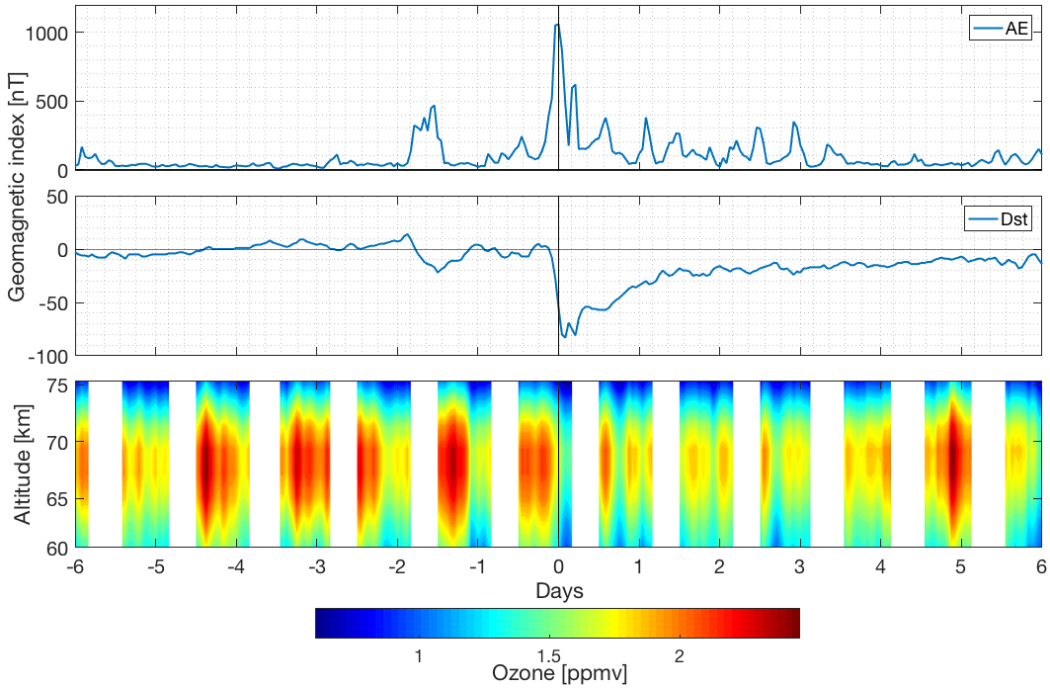

Figure 19: The two upper panels are the geomagnetic indices during the storm, showing six days prior and post peak. The bottom panel displays nightly ozone during the same time interval (white areas indicate daytime). All panels are centered on the AE index storm peak, thus visualizing the peak delay of the Dst compared to AE. The black vertical line indicates storm peak.

The upper panel in figure 19 shows the AE index six days prior and six days post storm peak. A smaller disturbance can be seen occurring 2 days before the main storm. The middle panel shows the Dst index, which mirrors the AE well for this particular storm. As both index panels are set in the AE storm peak reference frame, it is interesting to note that the Dst storm peak occurs some hours after the AE peak. The Dst index measured a disturbance of $-83\,\mathrm{nT}$, and the AE captured a value of $1058\,\mathrm{nT}$. The ozone response is shown in the bottom panel as a function of time and altitude. One can clearly observe the ozone ratio dropping in the days following the storm peak, and that the MMM seems to have recovered by day 5.

Figure 20 shows the same storm, but now centered in time on the Dst storm peak. Prior to the storm, the ozone column density oscillates around the normalized level of background ozone in a diurnal fashion. Almost immediately after the storm the ozone declines rapidly and reaches an epoch minimum. In the following days the ozone column density slowly increases and reaches pre-storm levels after 4 days.

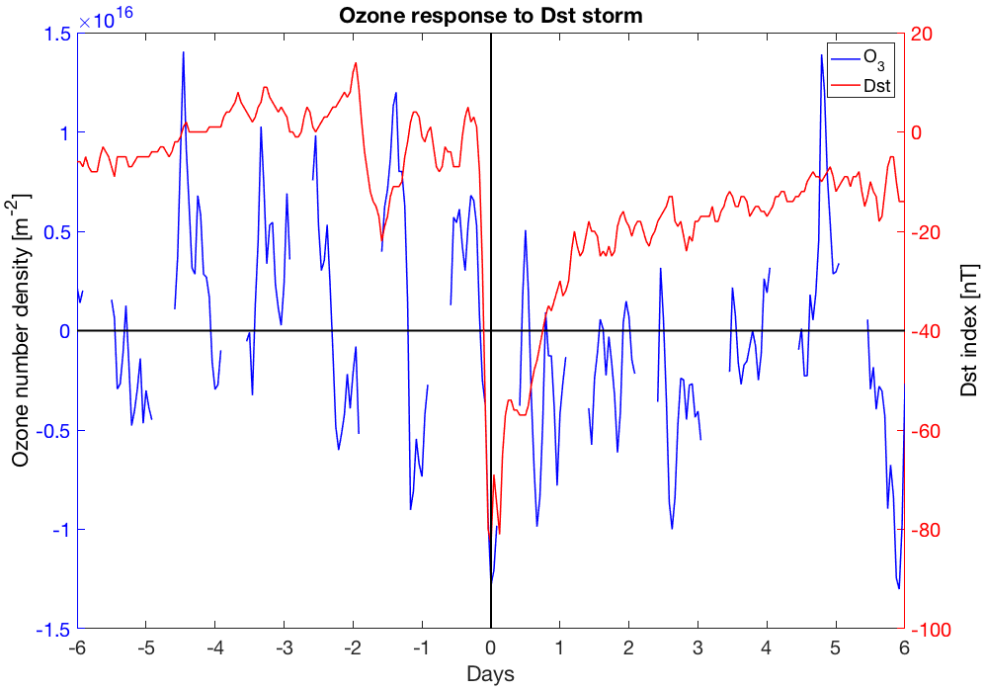

Figure 20: Dst index in red line and ozone column density in blue line. Ozone is adjusted for seasonal changes. The black horizontal line represents the background level of ozone and the black vertical line indicates hour of storm peak.

The gaps in the blue ozone line are due to removed daytime profiles or missing data during instrument downtime. The nighttime average ozone column was depleted by 239% relative to the six day average prior to the storm. The correlations between the ozone and the respective indices are shown in figure 21.

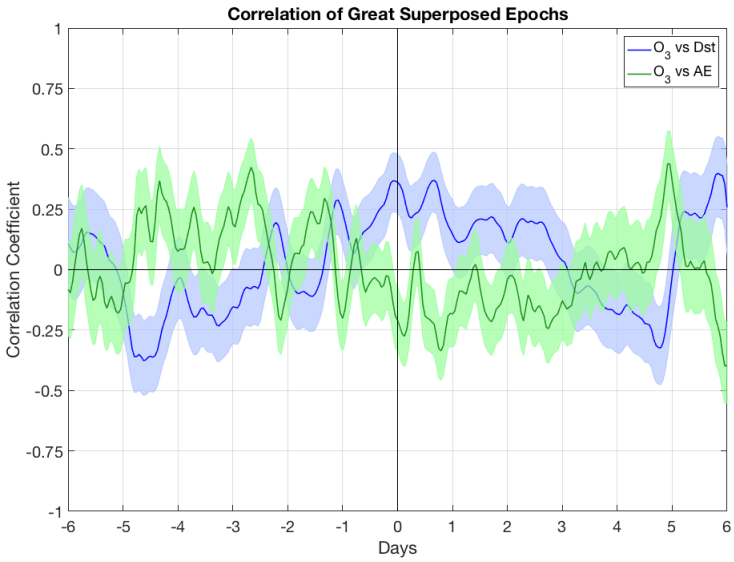

Figure 21: Correlation coefficients between O_3 and AE in green, and O_3 and Dst in blue. Shaded areas represent 95% confidence interval. Black vertical line indicates hour of storm peak.

The correlation of ozone and AE has no clear global peak which indicates that the AE index might not be suited as a representative of particle precipitation in the southern hemisphere. Dst on the other hand has a distinct maximum immediately following the Dst peak.

5.2 Superposed epoch analysis

For this superposed epoch analysis (SEA), key dates were defined as the hour of maximum AE value or minimum Dst value. Only isolated storms with quiet periods of five days post and prior to key date were chosen, since the ozone response from several successive storms is impossible to constrain. Quiet time is defined as AE values less than 400 nT4, and Dst values larger than -20 nT. The number of five days was selected based on two factors;

- Individual studies of storms and ozone responses indicated that the ozone partial column returns to normal levels within $\sim$ 4 days post storm, and a slightly longer interval is wanted to ensure stable ozone levels.
- A trade-off between the number of storms needed for a successful SEA, and wanting to capture indirect effects of particle precipitation.

Given an array of key dates, ozone and geomagnetic index time series were collected, centered on the key dates and averaged, creating the superposed epoch.

5.2.1 Storm categories

The value of the Dst and AE indices indicate the particle density in their respective current systems. We can therefore interpret the storm categories as the injecting of different amounts of particles into the upper-middle atmosphere. It is then logical to assume a certain amount of precipitating charged particles is needed to detect a statistically significant ozone reduction.

To pinpoint how strong a storm must be to have any detectable effect on mesospheric ozone, the list of key dates is divided into four storm categories. The categories (from weakest to strongest) are named: *minor*, *moderate*, *major* and *super*. Their lower and upper limits, and the number of events in each category, is presented in table 3.

Storm categories	**AE**		**Dst**	
	Storm limits	**# events**	**Storm limits**	**# events**
Minor	400-600 nT	17 (13)	-20 - -30 nT	26 (20)
Moderate	600-800 nT	22 (13)	-30 - -40 nT	16 (6)
Major	800-1000 nT	10 (7)	-40 - -50 nT	2 (2)
Super	1000 nT -	9 (4)	-50 nT -	11 (4)

Table 3: Overview of the storm categories for both AE and Dst index, with lower and upper storm limits as well as the number of events in each category. Numbers in parenthesis are the number of storms, excluding 2010.

The process of creating the superposed epoch is done individually for each storm category. For the two years of available ground based-data (2008-2009), each category was assigned a very low number of storms (see table 3), and the superposed epoch analysis suffered accordingly. To mitigate this, the following year was added to the dataset, which increased the number of events in each category significantly. The inclusion of 2010 was vital, as the solar cycle at that time started to rise back towards a new maximum which occurred in 2014, although with fewer sunspots than anticipated.

Although some geomagnetic activity is necessary, years close to or during a solar maximum is not well suited for this study. Very high levels of activity extends the auroral oval, and the precipitating area moves equatorwards and away from the location of the tertiary ozone maximum near the terminator. An optimal situation would be when the solar wind is powerful, with increased density and velocity, but with little disturbance to the auroral oval.

As can be understood from figures 16-18 and table 3, the AE and Dst indices do not always identify the same storms. This is to be expected; the AE index measures the effects of an increase in the ionospheric auroral electrojet current at high latitudes, while the Dst index measures effects by disturbances in the magnetospheric ring current at equatorial to mid latitudes (see chapter 2.3.3).

Figures 22 and 23 show the ozone response to EPP for all four storm classes, for both AE and Dst storm definitions.

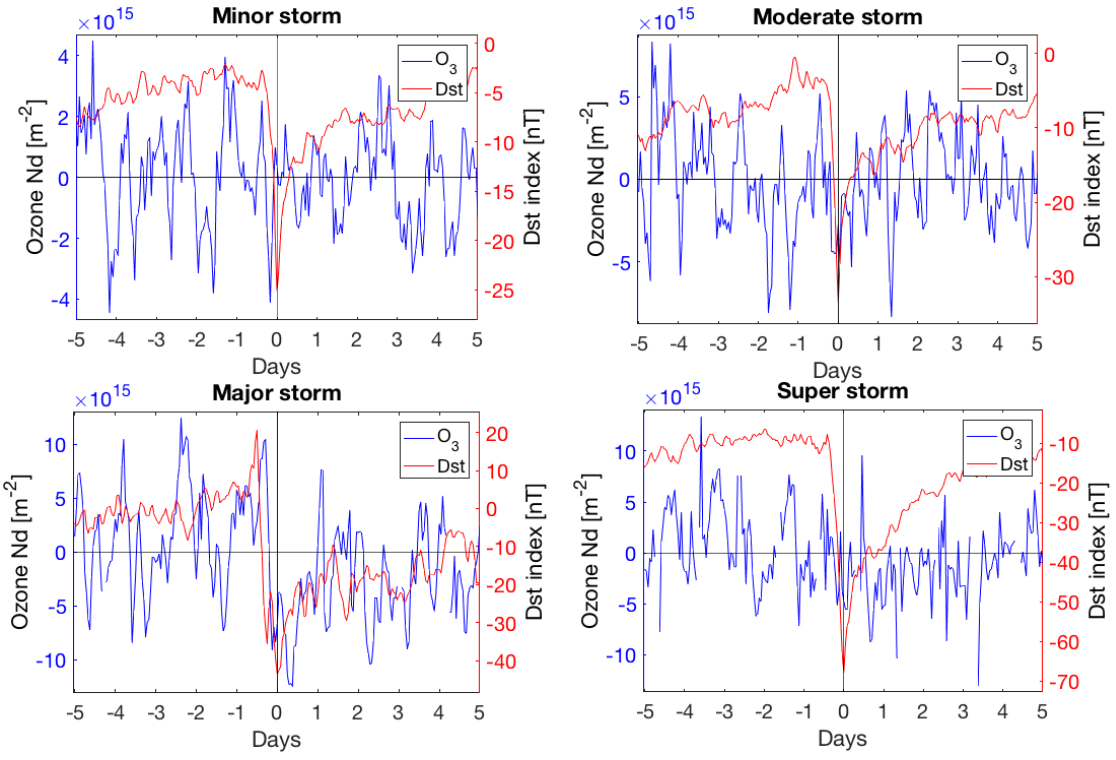

Figure 22: All four storm categories, from the *minor* storm epoch in top left corner to the *super* storm epoch in bottom right corner. Ozone in blue and geomagnetic index in red. Horizontal line represents the background level of ozone, vertical black line indicates storm peak.

For *minor* and *moderate* Dst storms, no depletion of ozone is visible. The limit of −40 nT for the moderate storm is extremely low, and such events are not usually counted as storms in most other, similar studies. As expected the MMM seems unperturbed by the slight increase in ring current activity. Immediately after a *major* storm however, a sharp decline in ozone column density is seen, reaching background levels after ∼1 day, before declining once more, although more slowly the second time. The second minimum is reached by day 3 and recovered to normal levels by day 4. Surprisingly no sudden decrease is seen in ozone levels during or after a *super* storm. However, the storm results in large negative Dst values for several days, and the ozone is consistently significantly lower than prior to the storm during this time, as seen in table 4.

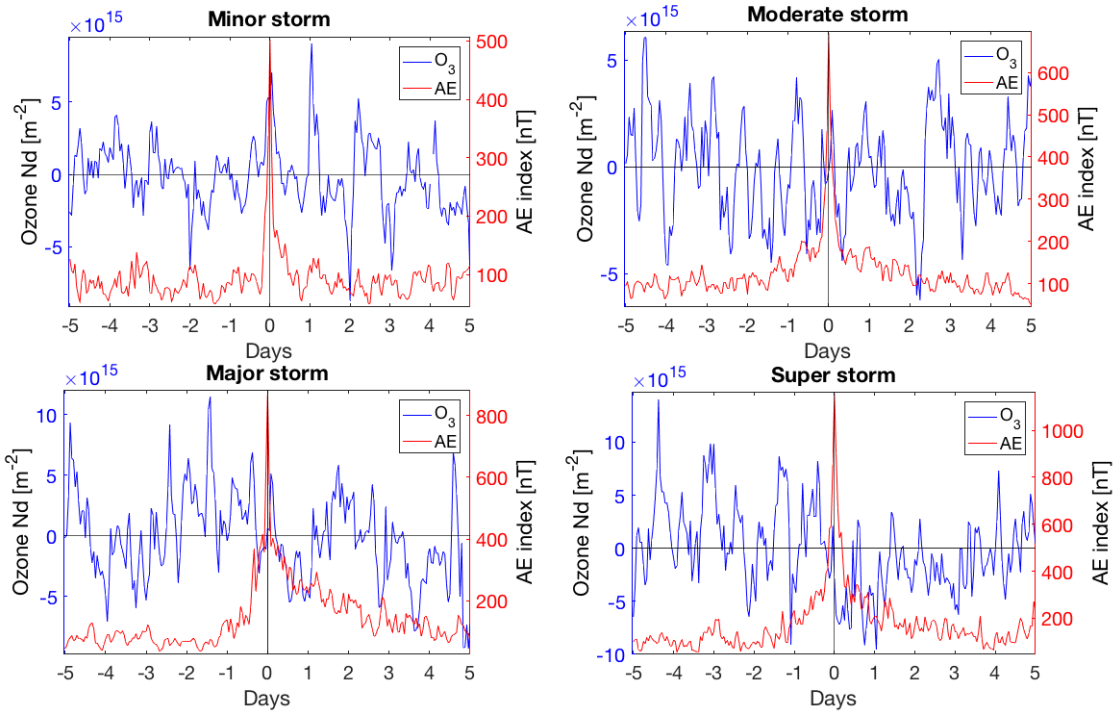

Figure 23: All four storm categories, from the *minor* storm epoch in top left corner to the *super* storm epoch in bottom right corner. Ozone in blue and geomagnetic index in red. Horizontal line represents the background level of ozone, vertical black line indicates storm peak.

For AE *minor* storms no immediate response is visible in figure 23. Ozone response to *moderate*, *major* and *super* storms seem to exhibit the same behaviour as the ozone response to Dst *major* storms. Within 24 hours of the AE storm peak, ozone is reduced to well below background values for the two strongest epochs. During the next 24 hours the ozone increases before a second depletion event occurs 2-3 days post peak. This second depletion also recovers within a few days. Even though the AE *moderate* storms exhibits the same behaviour in shape, the relative change in ozone actually increases slightly.

Great superposed epoch analysis

The quality of a superposed epoch analysis depends on a sufficient number of key dates. Satellite data for 2010 was added to the ground based observations for this specific reason. To further eliminate random background noise, the *major* and *super* epochs were combined for AE and Dst respectively, such that all storms above the lower *major* storm limit are joined to create one *great* superposed epoch with an increased number of key dates. The results from these *great* superposed epochs are presented in the figures 24 and 25.

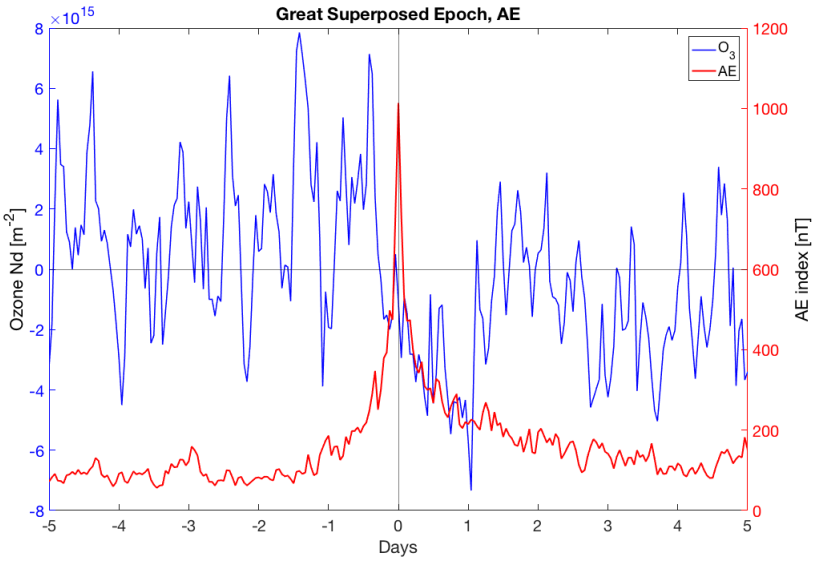

Figure 24: *Great* superposed epoch consisting of all *major* and *super* storms. Ozone in blue and AE in red, 5 days prior and 5 days post storm peak. The horizontal line represents the background level of ozone, the vertical black line indicates storm peak.

The *great* epoch for AE includes a total of 19 storms, all peaking above 800 nT. A large immediate ozone reduction following the AE storms is visible in figure 24. The depletion reaches its minimum after 24 hours, recovers rapidly during day two, but maintains a lower ozone level compared to pre-storm values for the five-day period.

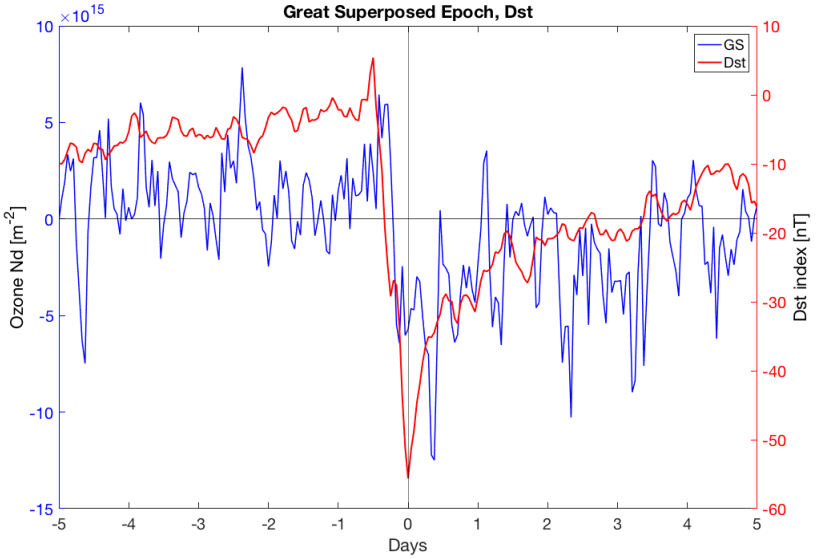

Figure 25: *Great* superposed epoch consisting of all *major* and *super* storms. Ozone in blue and Dst in red, 5 days prior and 5 days post storm peak. The horizontal line represents the background level of ozone, the vertical black line indicates storm peak.

The *great* epoch for Dst includes 13 storms, with a minimum value smaller than $-40\,\mathrm{nT}$. Similar to the *great* AE epoch, the *great* Dst epoch also experiences a sudden global minimum shortly after storm peak, although the minimum occurs only a few hours post storm peak for Dst. The sudden depletion mostly recovers by day two, but remains at slightly reduced levels for the remainder of the observed time period. The depletion appear to occur earlier in the Dst epoch compared to the AE epoch, but it is important to remember that the the Dst storm peak is delayed with respect to the AE peak (see figure 19), which cancels out at least some of this time-shift.

An overview of the relative decline in ozone levels for the different storm categories is given in table 4. The relative change is calculated from the climate adjusted partial column values between $60-75\,\mathrm{km}$. Column density values averaged over the five days following the storm peak is given in percentage relative to the 5-day average prior to the storm.

Storm categories	**AE**	**Dst**
Minor	-424%	-218%
Moderate	27%	36%
Major	-250%	-307%
Super	-216%	-264%
Great	-228%	-313%

Table 4: Relative O_3 depletion following storm peak for each of the main four storm categories, as well as the *great* super posed epoch which is the combined major and super storms.

Table 4 shows that the same overall trend is equal for the two indices; with the *major* storms having the largest impact on ozone column density. The similar pattern is likely due to the fact that the indices often report the same storms.

5.3 Correlation analysis

To quantify the strength of the relationship between particle precipitation and middle mesospheric ozone, a cross correlation analysis was performed. The correlation coefficient was calculated for all the storm classes for both AE and Dst, and can be seen in figures 26 and 27.

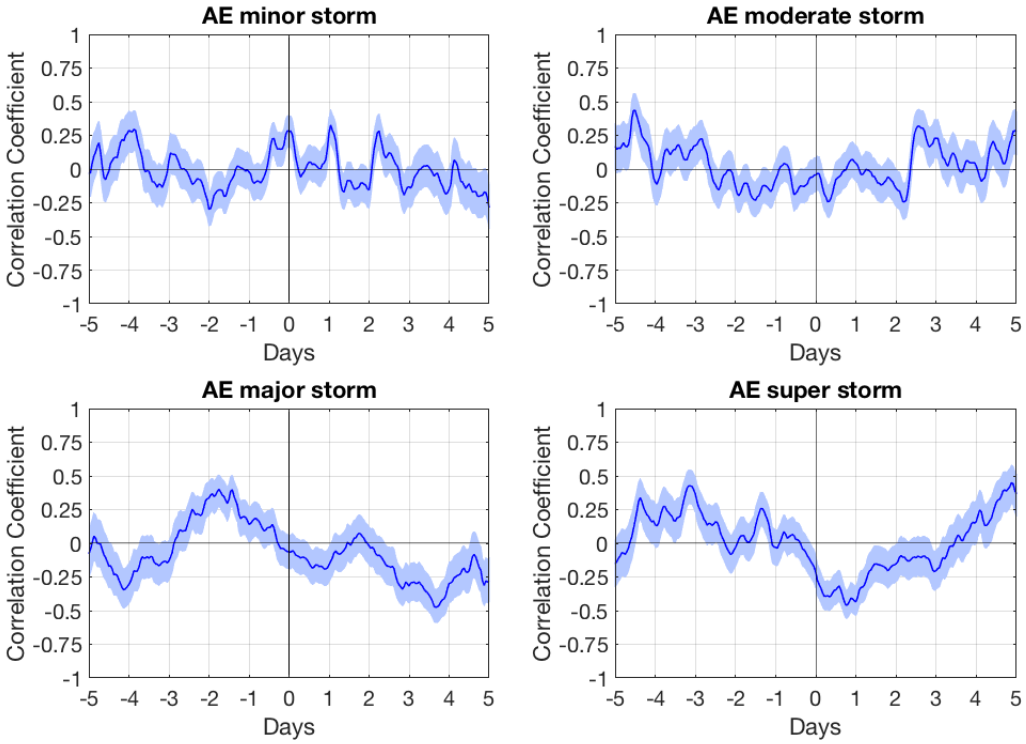

Figure 26: Correlation between the superposed epoch for each storm category of AE with O_3. Shaded area represents 95% confidence interval.

Figure 26 indicates that the correlation between the *minor*, *moderate* and *major* AE storms and O_3 are insignificant, in contrast to the the ozone partial column responses in figure 23. The AE *super* storms show a distinct negative peak at the expected time, yielding a coefficient of -0.46.

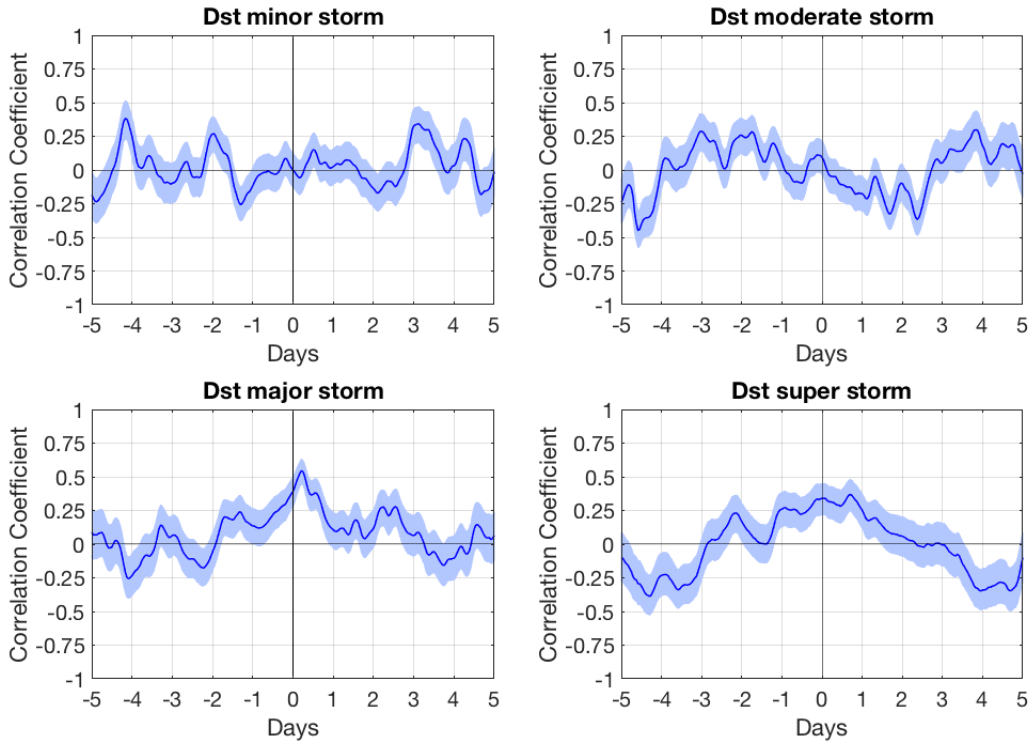

Figure 27: Correlation between the superposed epoch for each storm category of Dst with O_3. Shaded area represents 95% confidence interval.

The correlation coefficients between Dst *major* and *super* storms are 0.55 and 0.37 respectively. These results are more in line with the relative reductions in table 4.

As in section 5.2, the *great* superposed epochs are created by combining all *major* and *super* storms of Dst and AE respectively. Figure 28 depicts the correlation coefficients of the *great* superposed epochs for both AE and Dst storms with ozone.

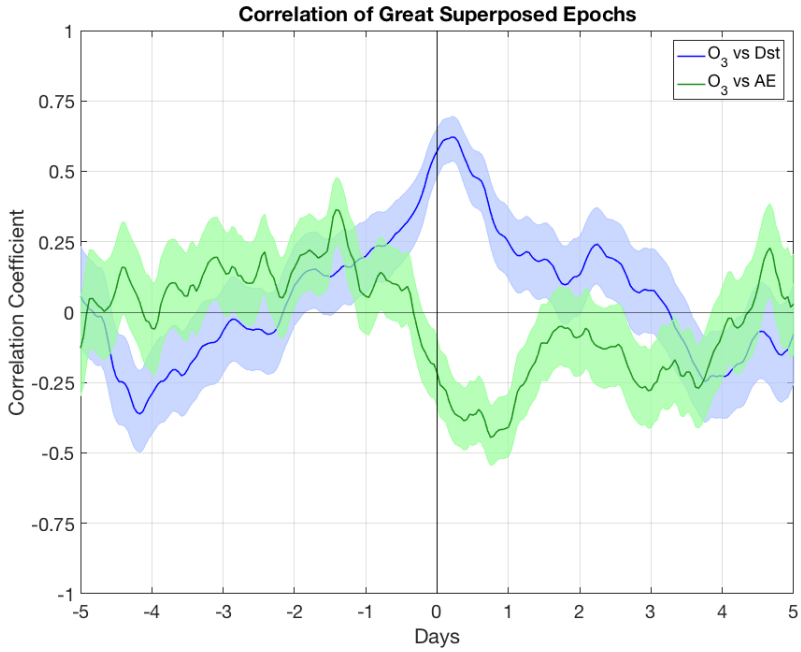

Figure 28: Correlation of *great* superposed epochs for Dst storm and O_3 in blue, and AE storm and O_3 in green. Shaded areas represent 95% confidence interval.

The correlation coefficient between the Dst *great* superposed epoch and O_3 is especially striking, reaching 0.62 (maximum coefficient for ozone and AE is 0.45). Note that the AE peak occurs ∼20 hours after the Dst peak. Auroral particles are less energetic than the radiation belt particles indirectly measured by the Dst index. The delayed peak of AE could indicate vertical transport of NO_x form higher altitudes where auroral particles ionize neutral species.

Good correlations do not indicate any cause and effect however, as there are many other variables that may have impacted the result. However, the purpose of a superposed epoch is to minimize the presence of random noise in the data. Seasonal variations were also accounted for by subtracting the background level of ozone.

5.4 Descension of ozone depletion

If ozone depletion is by reactions with either locally created or downward transported NO_x, one might expect to be able to trace a path of reduced ozone down toward the stratosphere (Daae et al., 2012). To check if this dynamics is observed in the dataset available in this work, the *great* superposed epochs were recalculated from $50-75$ km in intervals of 5 km descending through the atmosphere. The analysis was done for both Dst and AE. Figures 29 and 30 depicts the column integrated ozone number density of the intervals, showing a visible ozone depletion appearing almost immediately after the storm peak all the way down to ∼50 km.

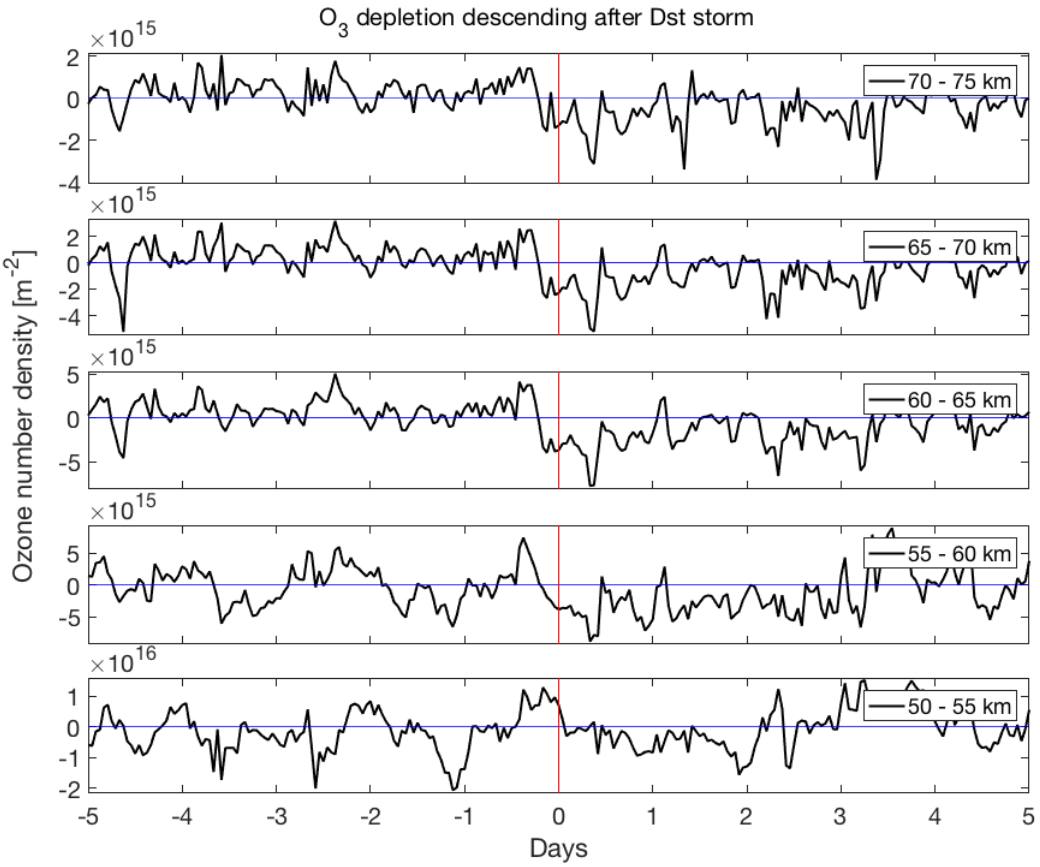

Figure 29: Partial columns of ozone between $50-75$ km in intervals of 5 km following *great* Dst storm. The blue horizontal line represents background level of ozone for given altitude interval, and the red vertical line indicates storm peak.

A sharp minimum is seen occurring less than 12 hours post Dst storm peak after *great* Dst storms. The dip appears at the same time for the four upper altitude intervals (from $75-55$ km). In the bottom panel ($50-55$ km), the same dip is no longer detectable, indicating the particles penetrate to no lower than ∼55 km

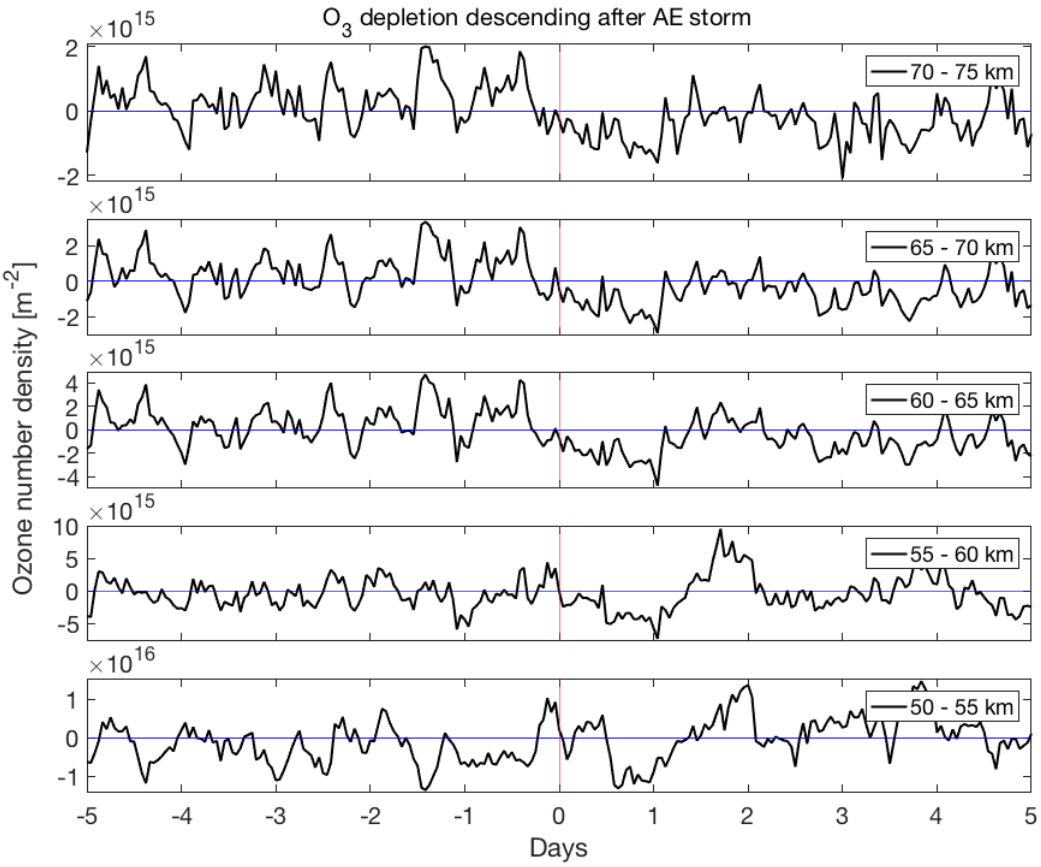

Figure 30: Partial columns of ozone between $50-75$ km in intervals of 5 km following *great* AE storm. The blue horizontal line represents background level of ozone for given altitude interval, and the red vertical line indicates storm peak.

A more gradual reduction of ozone is seen in figure 30, reaching its minimum after 24 hours. Similar to the Dst epochs, the minimum after the AE storm peak appears for the four upper panels at the same time, making RBP the most likely source for the creation of the catalytic species. The temporal diffusion of the depletion is smaller than what would be expected if NO_x was central to the reduction. Ozone levels recovered within 3-4 days for all altitude levels as previously seen for the MMM in figure both for the case study in figure 20 and for the superposed epoch in figures 25 and 24. The depleted zone is not seen to shift in time can either, indicating that the ozone is destroyed by HO_x rather than NO_x.

6 Discussion

The basis for this study was the depletion of middle mesospheric ozone following geomagnetic storms. 58 AE storms and 55 Dst storms were analyzed in total (many of the AE and Dst storms are the same however). The storms were categorized in storm classes according to their peak strength. A secondary objective was to investigate to what degree Dst and AE are useful tools for identification of key times of enhanced particle precipitation over Antarctica.

A case study was performed for a storm classified as a *super* storm by both indices, and its effect on mesospheric ozone can be seen in figures 19 and 20. Following this specific storm on the 22nd of July 2009, the ozone column density level dropped by -239% relative to the six day average prior to the storm, before recovering to normal levels within 4 days. Daae et al. (2012) studied this storm as well (their ozone analysis extended down to 50 km in altitude), and combined ozone profiles with NO observations in the altitude region $60-80$ km. The persistence of the ozone reduction at lower altitudes indicated a largely NO_x driven effect, although HO_x might still have played a role in the initial O_3 depletion. They concluded that the reduction of ozone was due to NO_x produced in the upper mesosphere and later transported downward, rather than NO_x of thermospheric origin. These findings supporting the claims in Smith et al. (2011), that the upwelling of air in the winter pole at $\sim$90 km prohibits the transport of trace species across the mesopause.

Superposed epoch analysis

Superposed epochs were created for all storm classes for both indices. As expected, there was little to no response following *minor* or *moderate* storm epochs by either index. The relative decrease calculated for *minor* storms (see table 4) seems large (-424%), but must be evaluated along with visual inspection of figure 23 and the correlation analysis in figure 26. When all is considered, the relationship between *minor* storms and ozone reduction is of little significance.

The *great* superposed epochs are the combined epochs of *major* and *super*storms. The sudden decrease in ozone levels following the injection of energetic particles can be seen to mostly recover over the course of 3-5 days for both indices, supporting the claim of Rohen et al. (2005) that ozone depletion above 50 km is generally governed primarily by the short lived catalytic cycle of HO_x, while O_3 losses below 50 km is driven by NO_x. If NO_x was more heavily involved at middle mesospheric altitudes, we would expect to observe a longer-lasting depletion, either stationary or moving downwards as time passes. Neither can be confirmed from the results in this study. In figures 29 and 30 the depletion is seen to immediately reach altitudes of $\sim$55 km, but the depleted zone shows very little diffusion in time, supporting an EPP-DE over EPP-IE. Odd-nitrogen could possibly have been transported horizontally out of the observed area, but it seems unlikely that this has

happened consistently at all altitudes for all observed storms.

The superposed epoch analysis was developed to identify
low-amplitude responses to external forcing. The method depends on a significant number of events, and even with the inclusion of ozone profiles from EOS Aura, the study would benefit from having an even larger O_3 database. The satellite data is not optimal for tracking ozone responses within the geographical constraints set by the location of the ground based instrument, as only one profile per day (or less) is available, which is not sufficient to capture the direct effects of particle precipitation. Therefore having another period with a ground based radiometer giving profiles with hourly time resolution would be beneficial.

Correlation analysis

AE *super* storms, and Dst *major* storms have the largest correlation coefficients, 0.55 and -0.46 for Dst and AE respectively. AE *major* storms gave only a coefficient of -0.18 at the expected time lag ∼24 hours after the storm, and a much larger peak ∼3.5 days following the storm coinciding with the large depression seen at the same time for *major* storms in figure 23. Dst *super* storms yielded a slightly worse coefficient (0.37) and the relative depletion after *super* storms was much lower than for *major* storms. This might be because the precipitating area is dependent on storm severity.

We know that during severely disturbed periods the slot between the two radiation belts can be filled with energetic particles, and the inner edge can expand towards the Earth. The relativistic particles that precipitate down through the loss cone gyrate along guiding field lines with footpoints too far south. As Rodger et al. (2007) showed during a 2005 storm, the precipitating particles originated from L=3 (footpoints at 55° MLAT), too far south for BAS to measure, and too far away from the terminator for the particles to interact directly with the MMM. The storms used by Rodger et al. (2007) measured $<-120\,\mathrm{nT}$ on the Dst scale, well within the *super* storm category of this study. NO_x produced at lower latitudes during *super* storms might be transported horizontally poleward, and could still affect the MMM indirectly after some time. Even though this is a possibility, no evidence of it is seen our data (see figures 29 and 30). It is also important to note that even though the Dst *major* storm epoch shows good correlation (0.55) and an extreme relative depletion (-307 %), only two storms make up this superposed epoch, compared to 11 storms in the *super* storm epoch (see table 3).

The great superposed epochs of AE and ozone are anti-correlated with correlation coefficients of -0.45 and -0.28, 18 hours and three days after storm peak respectively. The great superposed epochs of Dst and ozone are correlated with a coefficient of 0.62 six hours after the peak, and 0.24 two days after the peak.

AE and Dst as proxies for particle precipitation

It is commonly assumed that the aurora borealis in the northern hemisphere (NH) and the aurora australis in the southern hemisphere (SH) are mirror images of each other, and that the particles are evenly distributed between the two hemispheres from the plasma sheet in the equatorial plane of the magnetosphere. All Dst observatories are located close to the equator to measure the magnetic perturbations caused by an enhanced ring current. Rodger et al. (2007) showed that the ring current precipitation in the northern and southern hemispheres are indeed usually mirror images of each other.

The auroral electrojets are a very different type of current however, localized to the auroral ovals of their respective hemispheres. The AE index is derived from 12 observatories at auroral latitudes in the NH. AE calculations have thus only been performed with NH data as no similar coverage exists for the SH. The use of the AE index in this study is therefore questionable. A statistical study by Weygand et al. (2014) found that the NH-AE and SH-AE often display a strong correlation (mean coefficient of 0.65), indicating that NH-AE could be used as a proxy for SH particle precipitation. Differences do occur however, and using NH-AE to diagnose SH activity is far from optimal.

A study by Akasofu (1981) found that AE and Dst grow linearly together when the magnetosphere is moderately disturbed. For more severely disturbed periods, the AE index levels out, and even sometimes decreases. The reason suggested for this, is that as a storm progresses, the proportionality between energy input to the auroral electrojet and ring current changes. During the growth phase of a storm, the energy injections are close to equal giving the indices a linear dependence. After a while the auroral electrojet saturates, and so during the main phase most of the energy is injected into the ring current. Feldstein et al. (1997) argues that this deviation from a linear relationship during the main phase is because the auroral electrojets move equatorward as a storm evolves. As a result, the AE stations measuring the magnetic field disturbances are not anymore correctly located to conduct their measurements.

When Grafe and Feldstein (2000) looked into the relationship between AE and Dst, they found that the auroral electrojets can occur also during non-storm periods, without any ring current development. A close correlation between electrojet intensity and ring current intensity was therefore not found.

Other geomagnetic indices might be better suited; Kp and PC have observatories in both hemispheres. It would be interesting to investigate storms that appear in the AE index, but not in the Dst, and vice versa. That kind of study would improve our understanding of how the MMM is affected by different particle types (RBP and AP). It would also help to conclude about the suitability of AE as a proxy for particle precipitation in the southern hemisphere.

Another possible contributing factor to the difference in correlation between AE and O_3 and Dst and O_3 might be the different nature of the precipitating particles that AE and Dst measure the effects of. The AE is an indicator of low-energy auroral particles (AP), while the Dst indicates the precipitation of high-energy radiation belt particles (RBP). AP and RBP overlap when it comes to precipitation area, and from figure 10 we can see that they also (to some extent) overlap in ionizing altitude from $90 - 130$ km. However, RBP penetrate much further into the atmosphere where AP are not energetic enough to reach. As there are no solar proton events registered for 2008 and 2009, and only one for 2010 (August 14th, although the event did not trigger a storm on either of the AE or Dst

scales), we can assume that direct effects at 70 km must be due to RBP producing NO_x, HO_x or both. If any delayed effects are observed they could be from either AP or RBP, but then they must stem from NO_x as HO_x is destroyed within hours. From figures 29 and 30 no clear indication of transported NO_x can be seen, even though the effects of the particle precipitation are visible down to 55 km.

Instrument and method

Data gaps in the ground based measurements caused by the observation schedule are of little significance for the retrieval of ozone response to particle precipitation. The periods of the response is on a time scale of several hours to days, and is not affected much by a few hours of missing data from the ground based instrument. Some periods of instrument down-time due to maintenance (especially in Mai-June 2008 and 2009) could have been disruptive to the study. Luckily no storms of significance were identified during these time intervals. The one profile per day provided by satellite observations however is not optimal to study the highly dynamic middle mesospheric maximum.

The number of events is limited by the requirement of geomagnetic quiet-time prior to and following a storm. The decision of 5 days quiet time prior and post storm was a trade-off between number of storms for the SEA, and the wish of observing the MMM recovering in the aftermath of the storm. To observe long-term effects of the precipitation, a longer quiet-time period is required, which would in turn eliminate many storms. This can of course be mitigated if ozone data from additional years were added to the study. An extended period with measurements from a ground based radiometer providing hourly profiles would be preferable to additional satellite data.

The highest correlation between AE and O_3 occurs after approximately one day. The one day delay might be such that NO_x could be transported from $\sim$80 km, which was beyond the limit of the instruments used in this thesis. It might also be from the random distribution of storms throughout the day, as storms happening near dawn or during the day usually have the greatest effect on ozone during the following night.

To better understand the effects of particle precipitation on mesospheric ozone, particle type, energy distribution and precipitating area could be identified using measurements from NOAA satellites. Observations of NO and OH would also be useful to identify the degree of involvement of the different catalytic cycles.

The results of this work provide evidence to support the situation described by Rohen et al. (2005), where ozone loss above 50 km is driven primarily by the HO_x cycle. As only five days post storm peak is analyzed, this study is not very well suited to look for (longer lasting) effects of the long lived and transported NO_x.

7 Conclusion and future work

During polar winters, when the SZA is large for an extended period of time, the middle mesospheric ozone maximum appears near 70 km. It occurs close to the polar-night terminator where H_2O is no longer efficiently dissociated into hydroxyl due to high optical depths in the FUV. The aim of this study was to investigate whether a consistent relationship between particle precipitation and mesospheric ozone could be established using geomagnetic indices AE and Dst as proxies for the particle precipitation.

The ozone data was retrieved from the ground-based instrument BAS-MRT and the MLS instrument mounted on the EOS Aura satellite. A three year dataset of ozone profiles was used to create a background ozone climatology for each year, which was used to normalize the partial columns over the middle mesospheric maximum $60 - 75$ km) on a daily basis. Ten-day time series of normalized ozone, centered on the corresponding geomagnetic storm peak, were sorted into four storm classes according to peak storm strength for both AE and Dst indices (see table 3). A superposed epoch analysis was performed for each of the classes for both indices. The two strongest storm classes for each index showed a strong reduction in ozone following the storms, and were combined to create one *great* superposed epoch to further eliminate non-EPP induced variability in the ozone. The *great* superposed epochs resulted in a relative ozone reduction of -228% and -313% for AE and Dst respectively.

The correlation analysis gave the best results for AE *super* storms and Dst *major* storms. The weak correlation between Dst *super* storms and O_3 might be due to the nature of the precipitation of radiation belt particles, which might precipitate to latitudes southward of the observed area. Correlations between ozone and the *great* superposed epoch were high, with Dst yielding a coefficient of 0.62 (-0.45 for AE and O_3).

The study confirms that geomagnetic indices can indeed be used as proxies for particle precipitation. The equatorial ring current and its Dst index shows promising results as an indicator for particle precipitation and subsequent mesospheric ozone loss in both hemispheres. Usage of the northern hemisphere AE index for southern hemisphere particle precipitation is less suitable than using the Dst index, and might be the reason for the weaker correlation between AE and ozone.

No long term effects were investigated in this study, and there is little short-term evidence to support an indirect effect of transported NO_x originating from the thermosphere or upper mesosphere on the middle mesospheric maximum. The depletion occurs almost immediately after storm peak, supporting the conclusion that the effects seen on middle mesospheric ozone is due to radiation belt particles. For auroral particles to have a large effect on the MMM, NO_x created at higher altitudes must be transported down by way of the polar vortex down to the middle mesospheric maximum. This would result in a delayed (or prolonged effect, if HO_x was produced as well) depletion of a few days, which is not observed in this data set. There is almost no temporal diffusion of the ozone reduction. At altitudes where auroral particles dominate the ionizing landscape (see figure

10), Smith et al. (2011) report a reverse dynamic cell causing not downward, but upward transport of trace species, which makes downward transport of thermospheric NO_x unlikely.

The results indicate that the observed ozone depletion was mainly due to energetic radiation belt particles creating odd-hydrogen which in turn catalytically destroyed ozone in the altitude region $55-75$ km. To further understand the interactions between energetic particle precipitation and middle mesospheric ozone, data from other winter seasons with hourly time resolution from ground-based instruments providing profiles of NO, OH and O_3 are required. Satellites providing information on particle energies and precipitating area would also be useful. This study has showed that moderate geomagnetic events, which occur frequently even during solar minimum, have a significant effect on ozone in the middle mesosphere, and ozone is reduced at stratospheric altitudes as well.

Bibliography

Akasofu, S.-I. (1981). Relationships between the ae and dst indices during geomagnetic storms. *Journal of Geophysical Research: Space Physics*, 86(A6):4820–4822. 6

Andrews, D. G. (2010). *An Introduction to Atmospheric Physics*. Cambridge University Press. 2.1, 2.2.1

Baker, D., Erickson, P., Fennell, J., Foster, J., Jaynes, A., and Verronen, P. (2018). Space weather effects in the earth's radiation belts. *Space Science Reviews*, 214(1):17. 2.3.2

Baliukin, I. I., Bertaux, J.-L., Quémerais, E., Izmodenov, V., and Schmidt, W. (2019). Swan/soho lyman-α mapping: the hydrogen geocorona extends well beyond the moon. *Journal of Geophysical Research: Space Physics*. 2.1.2

Barth, C. A. (1992). Nitric oxide in the lower thermosphere. *Planetary and space science*, 40(2-3):315–336. 2.4.1

BAS (2018). British Antarctic Survey. `https://www.bas.ac.uk`. 2.2

Bönisch, H., Engel, A., Birner, T., Hoor, P., Tarasick, D., and Ray, E. (2011). On the structural changes in the brewer-dobson circulation after 2000. *Atmospheric Chemistry and Physics*, 11(8):3937–3948. 2

Collard, H. R., Mihalov, J. D., and Wolfe, J. H. (1982). Radial variation of the solar wind speed between 1 and 15 au. *Journal of Geophysical Research: Space Physics*, 87(A4):2203–2214. 2.3.1

Daae, M., Espy, P., Tyssøy, H. N., Newnham, D., Stadsnes, J., and Søraas, F. (2012). The effect of energetic electron precipitation on middle mesospheric night-time ozone during and after a moderate geomagnetic storm. *Geophysical Research Letters*, 39(21). 1, 5.4, 6

Daae, M., Straub, C., Espy, P. J., and Newnham, D. (2013). Atmospheric ozone above troll station, antarctica observed by a ground based microwave radiometer. *Earth System Science Data Discussions*, 6(2). 1, 3.1, 4

Data Analysis Center for Geomagnetism and Space Magnetism (2015). World Data Center for Geomagnetism, Kyoto. `http://wdc.kugi.kyoto-u.ac.jp/index.html`. 3.3, 3.3.1, 4.2

Davis, N. and Sugiura, M. (1966). Auroral electrojet activity index ae and its universal time variations. *Journal of Geophysical Research*, 71(3):785–801. 3.3.1

Dobson, G. M. B., Harrison, D., and Lawrence, J. (1929). Measurements of the amount of ozone in the earth's atmosphere and its relation to other geophysical conditions.—part iii. *Proceedings of the Royal Society of London. Series A, Containing Papers of a Mathematical and Physical Character*, 122(790):456–486. 2.1.3

Eastwood, J., Hietala, H., Toth, G., Phan, T., and Fujimoto, M. (2015). What controls the structure and dynamics of earth's magnetosphere? *Space Science Reviews*, 188(1-4):251–286. 7

Ebert, R., McComas, D., Elliott, H., Forsyth, R., and Gosling, J. (2009). Bulk properties of the slow and fast solar wind and interplanetary coronal mass ejections measured by ulysses: Three polar orbits of observations. *Journal of Geophysical Research: Space Physics*, 114(A1). 2.3.1, 2

Feldman, U., Landi, E., and Schwadron, N. (2005). On the sources of fast and slow solar wind. *Journal of Geophysical Research: Space Physics*, 110(A7). 2.3.1

Feldstein, Y. I., Grafe, A., Gromova, L., and Popov, V. (1997). Auroral electrojets during geomagnetic storms. *Journal of Geophysical Research: Space Physics*, 102(A7):14223–14235. 6

Fitzpatrick, R. (2014). *Plasma Physics*. CRC Press, Taylor & Francis Group. 2.3, 2.3.3

Froidevaux, L., Read, W., Lungu, T., Cofield, R., Fishbein, E., Flower, D., Jarnot, R., Ridenoure, B., Shippony, Z., Waters, J., et al. (1996). Validation of uars microwave limb sounder ozone measurements. *Journal of Geophysical Research: Atmospheres*, 101(D6):10017–10060. 2.2

Funke, B., López-Puertas, M., Gil-López, S., Von Clarmann, T., Stiller, G., Fischer, H., and Kellmann, S. (2005). Downward transport of upper atmospheric nox into the polar stratosphere and lower mesosphere during the antarctic 2003 and arctic 2002/2003 winters. *Journal of Geophysical Research: Atmospheres*, 110(D24). 2.2.3

Gibson, S., Kozyra, J., de Toma, G., Emery, B., Onsager, T., and Thompson, B. (2009). If the sun is so quiet, why is the earth ringing? a comparison of two solar minimum intervals. *Journal of Geophysical Research: Space Physics*, 114(A9). 4.2

Grafe, A. and Feldstein, Y. (2000). About the relationship between auroral electrojets and ring currents. In *Annales Geophysicae*, volume 18, pages 874–886. Springer. 6

Hartogh, P., Jarchow, C., Sonnemann, G., and Grygalashvyly, M. (2004). On the spatiotemporal behavior of ozone within the upper mesosphere/mesopause region under nearly polar night conditions. *Journal of Geophysical Research: Atmospheres*, 109(D18). 1, 6, 2.2.2, 2.2.2

Hendrickx, K. (2018). *Solar forcing on Nitric Oxide in the upper atmosphere*. PhD thesis, Stockholm University. 11

Hendrickx, K., Megner, L., Marsh, D. R., Gumbel, J., Strandberg, R., and Martinsson, F. (2017). Relative importance of nitric oxide physical drivers in the lower thermosphere. *Geophysical Research Letters*, 44(19):10–081. 2.4.1

International Services of Geomagnetic Indices (2013). IAGA Endorsed Geomagnetic Indices. `http://isgi.unistra.fr/index.php`. 4.2

Jackman, C. H., Roble, R. G., and Fleming, E. L. (2007). Mesospheric dynamical changes induced by the solar proton events in october–november 2003. *Geophysical Research Letters*, 34(4). 1

Kivelson, M. G. and Russel, C. T. (1995). *Introduction to Space Physics*. Press Syndicate of the University of Cambridge. 2.3, 2.3.1

Kleinknecht, N. (2015). Millimeter-wave radiometer observations of middle atmosphere ozone in antarctica. Master's thesis, Technosche Universität München. 4, 3.1

Livesey, N. J., Read, W. G., Froidevaux, L., Lambert, A., Manney, G. L., Pumphrey, H. C., Santee, M. L., Schwartz, M. J., Wang, S., Cofield, R. E., et al. (2011). Version 3.3 level 2 data quality and description document. *JPL D-33509*. 3.2, 4.1

Marsh, D., Smith, A., Brasseur, G., Kaufmann, M., and Grossmann, K. (2001). The existence of a tertiary ozone maximum in the high-latitude middle mesosphere. *Geophysical Research Letters*, 28(24):4531–4534. 1, 2.2, 3, 2.2.1

Minschwaner, K., Manney, G., Wang, S., and Harwood, R. (2011). Hydroxyl in the stratosphere and mesosphere-part 1: Diurnal variability. *Atmospheric Chemistry and Physics*, 11(3):955. 2.2.1

Mironova, I. A., Aplin, K. L., Arnold, F., Bazilevskaya, G. A., Harrison, R. G., Krivolutsky, A. A., Nicoll, K. A., Rozanov, E. V., Turunen, E., and Usoskin, I. G. (2015). Energetic particle influence on the earth's atmosphere. *Space science reviews*, 194(1-4):1–96. 10

Philips, T. (2009). SpaceWeather. `http://spaceweather.com/archive.php`. 17

Potemra, T. (1983). Magnetospheric currents. *John Hopkins APL Technical Digest*, 4(4):846–854. 2.3.3

Prölss, G. W. (2004). *Physics of the Earth's Space Environment*. Springer. 2.3

Randall, C., Harvey, V. L., Siskind, D., France, J., Bernath, P., Boone, C., and Walker, K. (2009). Nox descent in the arctic middle atmosphere in early 2009. *Geophysical Research Letters*, 36(18). 2.4.1

Rodger, C. J., Clilverd, M. A., Thomson, N. R., Gamble, R. J., Seppälä, A., Turunen, E., Meredith, N. P., Parrot, M., Sauvaud, J.-A., and Berthelier, J.-J. (2007). Radiation belt electron precipitation into the atmosphere: Recovery from a geomagnetic storm. *Journal of Geophysical Research: Space Physics*, 112(A11). 6

Rohen, G., Von Savigny, C., Sinnhuber, M., Llewellyn, E., Kaiser, J., Jackman, C., Kallenrode, M.-B., Schröter, J., Eichmann, K.-U., Bovensmann, H., et al. (2005). Ozone depletion during the solar proton events of october/november 2003 as seen by sciamachy. *Journal of Geophysical Research: Space Physics*, 110(A9). 2.4.1, 6

Sinnhuber, M., Nieder, H., and Wieters, N. (2012). Energetic particle precipitation and the chemistry of the mesosphere/lower thermosphere. *Surveys in Geophysics*, 33(6):1281–1334. 2.2.1, 2.4.1

Smith, A. (2012). Interactions between the lower, middle and upper atmosphere. *Space Sci Revieww*, 168:1–21. 2.2.3

Smith, A., Garcia, Rolando Marsh, D., and Richter, J. (2011). Waccm simulations of the mean circulation and trace species transport in the winter mesosphere. *Journal of Geophysical Research*, 116:4. 2.1.3, 2.2.3, 6, 7

Smith, A. K., Espy, P. J., López-Puertas, M., and Tweedy, O. V. (2018). Spatial and temporal structure of the tertiary ozone maximum in the polar winter mesosphere. *Journal of Geophysical Research: Atmospheres*, 123(8):4373–4389. 1, 2.2.3

Sofieva, V., Kyrölä, E., Verronen, P., Seppälä, A., Tamminen, J., Marsh, D., Smith, A., Bertaux, J.-L., Hauchecorne, A., Dalaudier, F., et al. (2009). Spatio-temporal observations of the tertiary ozone maximum. *Atmospheric Chemistry and Physics*, 9(13):4439–4445. 1, 2.4.1

Sonnemann, G., Grygalashvyly, M., Hartogh, P., and Jarchow, C. (2006). Behavior of mesospheric ozone under nearly polar night conditions. *Advances in Space Research*, 38(11):2402–2407. 5, 2.2.2

Sonnemann, G. R., Hartogh, P., Jarchow, C., Grygalashvyly, M., and Berger, U. (2007). On the winter anomaly of the night-to-day ratio of ozone in the middle to upper mesosphere in middle to high latitudes. *Advances in Space Research*, 40(6):846–854. 4.1

Thorne, R. M. (1980). The importance of energetic particle precipitation on the chemical composition of the middle atmosphere. *pure and applied geophysics*, 118(1):128–151. 9

Verronen, P. T., Seppälä, A., Kyrölä, E., Tamminen, J., Pickett, H. M., and Turunen, E. (2006). Production of odd hydrogen in the mesosphere during the january 2005 solar proton event. *Geophysical Research Letters*, 33(24). 1

Weygand, J., Zesta, E., and Troshichev, O. (2014). Auroral electrojet indices in the northern and southern hemispheres: a statistical comparison. *Journal of Geophysical Research: Space Physics*, 119(6):4819–4840. 6

Xiong, C., Lühr, H., Wang, H., and Johnsen, M. G. (2014). Determining the boundaries of the auroral oval from champ field-aligned current signatures-part 1. *Annales Geophysicae*, 32:609–622. 3.1

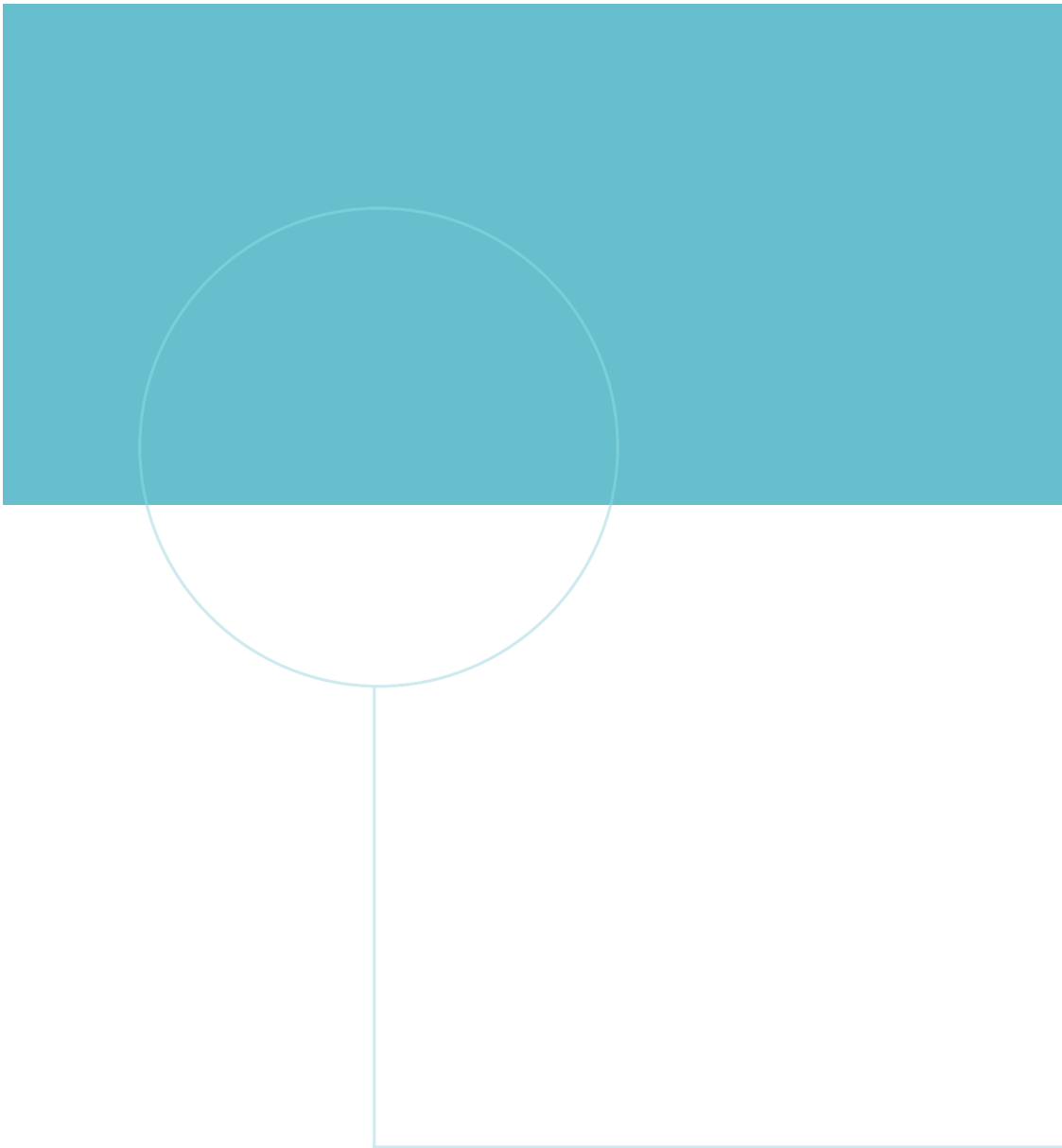

NTNU
Norwegian University of
Science and Technology